

The Warm-Core Structure of Hurricane Earl (2010)

DANIEL P. STERN

University Corporation for Atmospheric Research, Monterey, California

FUQING ZHANG

Department of Meteorology, The Pennsylvania State University, University Park, Pennsylvania

(Manuscript received 2 November 2015, in final form 24 March 2016)

ABSTRACT

The warm-core structure of Hurricane Earl (2010) is examined on four different days, spanning periods of both rapid intensification (RI) and weakening, using high-altitude dropsondes from both the inner core and the environment, as well as a convection-permitting numerical forecast. During RI, strong warming occurred at all heights, while during rapid weakening, little temperature change was observed, implying the likelihood of substantial (unobserved) cooling above flight level (12 km). Using a local environmental reference state yields a perturbation temperature profile with two distinct maxima of approximately equal magnitude: one at 4–6-km and the other at 9–12-km height. However, using a climatological-mean sounding instead results in the upper-level maximum being substantially stronger than the midlevel maximum. This difference results from the fact that the local environment of Earl was warmer than the climatological mean and that this relative warmth increased with height. There is no obvious systematic relationship between the height of the warm core and either intensity or intensity change for either reference state.

The structure of the warm core simulated by the convection-permitting forecast compares well with the observations for the periods encompassing RI. Later, an eyewall replacement cycle went unforecast, and increased errors in the warm-core structure are likely related to errors in the forecast wind structure. At most times, the simulated radius of maximum winds (RMW) had too great of an outward slope (the upper-level RMW was too large), and this is likely also associated with structural biases in the warm core.

1. Introduction

One of the most distinguishing characteristics of tropical cyclones (TCs) is that the temperature within the eye is warmer than the ambient environment: that is, TCs are “warm core” vortices. Consistent with thermal wind balance, this negative radial temperature gradient is associated with the horizontal winds having a maximum at low levels and decreasing upward. Three pioneering studies in the 1960s and 1970s used flight-level measurements at multiple levels to investigate the radial and vertical structure of the warm core (La Seur and Hawkins 1963; Hawkins and

Rubsam 1968; Hawkins and Imbembo 1976). Using the annual mean Caribbean sounding of Jordan (1958) to define the environment, the above studies found that the maximum perturbation temperature was near 250–300 mb (1 mb = 1 hPa) in Hurricanes Cleo (1958) and Hilda (1964), although in Hurricane Inez (1966) there were two distinct maxima, with the lower one occurring near 600–650 mb. This midlevel maximum was believed to be “rather unusual.” Stern and Nolan (2012, hereinafter SN12) and Stern and Zhang (2013a, b, hereinafter SZ13a,b) used idealized simulations to investigate the structure of the warm core and found a consistent midlevel (4–8 km) maximum. This result was robust to varying the microphysics, the storm size, and the presence or absence of environmental mean flow and vertical wind shear. Furthermore, this midlevel maximum occurred across a wide range of intensities, from category 1 to category 5.

Corresponding author address: Daniel P. Stern, University Corporation for Atmospheric Research, 7 Grace Hopper Ave., Monterey, CA 93943.
E-mail: dstern@ucar.edu

A different perspective on the warm core is seen in a series of studies by [Chen et al. \(2011\)](#) and [Chen and Zhang \(2013\)](#), who examined a simulation of Hurricane Wilma (2005). They found an upper-level (14 km) maximum in perturbation temperature in their simulation and argued that the height of this warming caused Wilma to be more intense than it would have been otherwise. They also argued that the formation of the upper-level warm core helped to trigger rapid intensification (RI). As we will discuss later, we do not believe that attribution of intensity to warm-core height is valid.

In a simulation of Supertyphoon Megi (2010), [Wang and Wang \(2014\)](#) found two prominent maxima in perturbation temperature: one at midlevels (5–6 km) and another at upper levels (15–16 km). The upper-level maximum did not form until a period of RI began (the intensity was already category 2 at this point, however), and thereafter the greatest warming was at upper levels, with a slight lowering of the height of the maximum with time during RI (from about 16 to 15 km). As in [Chen and Zhang \(2013\)](#), [Wang and Wang \(2014\)](#) attributed the upper-level warming in part to detrainment and compensating descent from convective bursts that penetrate the stratosphere.

In an idealized simulation, [Ohno and Satoh \(2015\)](#) simulated a TC in an environment of radiative convective equilibrium with an SST of 31°C. For much of the period of intensification, the maximum perturbation temperature was found at about 9-km height. Once the storm had deepened to about 950 mb, a separate maximum formed at about 16-km height, nearly coincident with the environmental tropopause. This tropopause maximum became dominant, and the 9-km maximum eventually weakened in magnitude and merged with the tropopause maximum. At quasi-steady intensity (about 900 mb), there was a single maximum at about 15-km height.

Taken together, a number of recent numerical studies indicate that distinct mid- and upper-level maxima in perturbation temperature may occur within the eye of tropical cyclones. In [Wang and Wang \(2014\)](#) and [Ohno and Satoh \(2015\)](#), the upper-level maximum did not form until the TC became relatively intense (category 2 or 3). This is broadly consistent with [SN12](#), where a secondary upper-level (12–14 km) maximum was found in many idealized simulations, and this maximum only occurred after the simulated TCs were approximately category-3 hurricanes. Unlike in [Wang and Wang \(2014\)](#) and [Ohno and Satoh \(2015\)](#), the upper-level maxima in the simulations of [SN12](#) were generally weaker in magnitude than the midlevel (4–8 km) maxima, and the upper-level maxima were also not as persistent.

As discussed in [SN12](#), there is a commonly held belief that the warm core is (and should be) maximized in the upper troposphere. Since the 1960s, there have been relatively few flights into TCs above 6-km height, and so [SN12](#) argued that the typical structure of the warm core is not actually well known. There have been several field programs organized by NASA that involve high-altitude aircraft flying into or above the inner cores of TCs. [Halverson et al. \(2006\)](#) documented the warm-core structure of Hurricane Erin (2001), using a combination of sondes dropped by the DC-8 (~11–12-km height) and ER-2 (~19-km height) aircraft over a 4-h period on 10 September. One ER-2 sonde was dropped within the eye, and [Halverson et al. \(2006\)](#) found the perturbation temperature (using a local environmental reference state) to be greatest near 500 mb (11°C) but nearly uniform (near 9°C) from 750 to 300 mb. Erin was rapidly weakening at the time it was sampled, and the authors attributed the existence of the midlevel maximum to the weakening of convection but also attributed the weakening of the storm intensity to the removal of the upper-level warm core by vertical wind shear. In a numerical simulation of Erin, [Wu et al. \(2006\)](#) found that the simulated warm-core maximum was similar in its magnitude and height to the observed warm core. However, they did not examine the hypothesis of [Halverson et al. \(2006\)](#) that the warm-core maximum lowered as the storm weakened.

[Durden \(2013\)](#) compiled and analyzed 18 eye soundings from high-altitude dropsondes (9 storms on 16 different days), as well as 9 soundings from surface-based radiosondes (9 storms on 9 different days). [Durden \(2013\)](#) found a wide variation in the height of the maximum perturbation temperature among the eye soundings, ranging from 750 to 250 mb. In addition, this study reveals a tendency for this height to increase with increasing warm-core magnitude, although the variance in the data is quite large; see Fig. 2 of [Durden \(2013\)](#). [Durden \(2013\)](#) also showed that the height of the maximum can be sensitive to the chosen environmental reference profile, which is consistent with the idealized simulations of [SN12](#).

The goal of this study is to improve our observational understanding of the warm core using high-altitude dropsondes released in and near the eye of Hurricane Earl (2010). Additionally, we complement our observational analyses by investigating the structure and evolution of the warm core in a high-resolution simulation of Earl. Earl is one of the most intensively sampled storms yet observed, having been investigated by six different aircraft. Earl is also distinctive in that high-altitude observations are available throughout much of its life cycle, including both periods of rapid

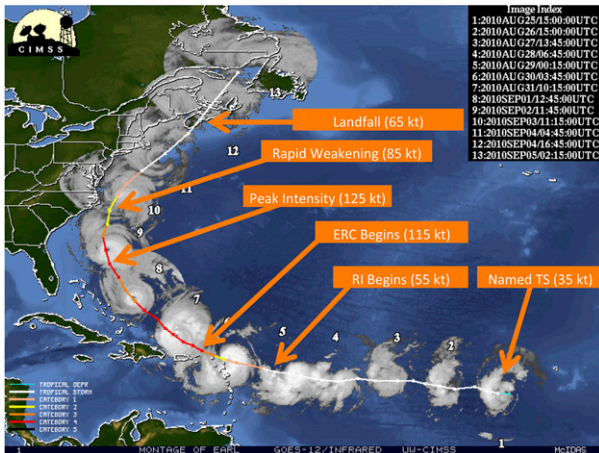


FIG. 1. Satellite montage illustrating the track, intensity, and structure of Earl. Figure adapted from an image that is courtesy of University of Wisconsin/CIMSS.

intensification and rapid weakening. We hope that, through the analysis of this unique dataset, we will be able to clarify some of these outstanding questions regarding the structure and influence of the warm core: in particular,

- (i) Is there a relationship between the height of the maximum perturbation temperature and either the intensity or intensity tendency?
- (ii) Is the height of maximum perturbation temperature sensitive to the choice of reference profile?
- (iii) Is it possible to relate structural changes in the wind field to changes in the height of the warm core?

2. Overview of Earl and evolution of the wind field

a. Overview of Hurricane Earl (2010)

Hurricane Earl was an intense tropical cyclone that developed from an easterly wave that emerged from the west coast of Africa on 23 August. Earl became a named storm at 1200 UTC 25 August and a hurricane at 1200 UTC 29 August (Cangialosi 2011). To illustrate the evolution of Earl, Fig. 1 shows a satellite montage of Earl with the track overlaid, produced by the University of Wisconsin/Cooperative Institute for Meteorological Satellite Studies (CIMSS). During the first few days of its lifetime, Earl moved westward at 15–20 kt ($1 \text{ kt} = 0.51 \text{ m s}^{-1}$) to the south of a strong subtropical ridge. On 29 August, the translation speed slowed down; Earl began moving northwestward and underwent a 36-h period of RI that began at 0600 UTC 29 August. The maximum wind speed (V_{max}) increased by 40 kt (from 75 to 115 kt) over the 24-h period ending at 1800 UTC 30 August, at which

time an eyewall replacement cycle (ERC) began. In association with the ERC, Earl weakened slightly to 105 kt at 0600 UTC 1 September but then began to reintensify and achieved its peak intensity of 125 kt 24 h later (0600 UTC 2 September), while located about 700 km southeast of Wilmington, North Carolina. Shortly following peak intensity, Earl rapidly weakened, to 100 kt at 1800 UTC 2 September, 85 kt at 0600 UTC 3 September, and 60 kt at 0000 UTC 4 September. The National Hurricane Center (NHC) attributed this rapid weakening to a combination of another ERC, cooler SSTs, stronger shear, and a drier environment (Cangialosi 2011). After one more period of slight intensification, Earl made landfall at 1500 UTC 4 September as a 65-kt hurricane in Nova Scotia.

b. Evolution of the wind field

Prior to analyzing the warm core in section 3, here we first examine the evolution of the wind field. Later, in section 4, we will compare the observed wind structure to that of a simulation and, from this comparison, infer potential relationships between biases in the wind field and biases in the warm-core structure. Two NOAA P-3 aircraft sampled Earl during 11 different missions from 28 August until 4 September. Here, we examine the evolution of the wind field as measured by the tail Doppler radar during eight of these flights, encompassing the period from approximately 1200 UTC on 29 August to 0000 UTC on 3 September. For each flight, the P-3 flew two to four radial legs through the storm center, and for each leg, NOAA's Hurricane Research Division (HRD) performed a three-dimensional analysis of the Cartesian horizontal (u and v) and vertical (w) velocities, using the automated technique of Gamache et al. (2004). We acquired these analyses, averaged all legs from each flight to maximize azimuthal coverage, and calculated the tangential winds (v_t) from u and v . For Earl, the analyses were produced at 5-km horizontal grid spacing, although the intrinsic resolution of the radar is finer than this (Jorgensen et al. 1983; Reasor et al. 2009). Note that the analyses we present below are quite similar to those of Rogers et al. (2015) for the four periods that overlap, except that Rogers et al. (2015) used a finer analysis (2-km horizontal grid spacing).

Figure 2 shows the horizontal wind speed at 2-km height for each of the eight flights. Figure 3 shows radius–height plots of the azimuthal mean tangential wind, with the radius of maximum wind (RMW) indicated. For each flight, we refer to the approximate central time of the legs used in the averaging, which occur over a 2–4-h period. The first flight was centered at 1100 UTC 29 August; at this time, RI had just begun, and Earl was a category-1 (65 kt) hurricane. The wind field was very broad and asymmetric, with the region of

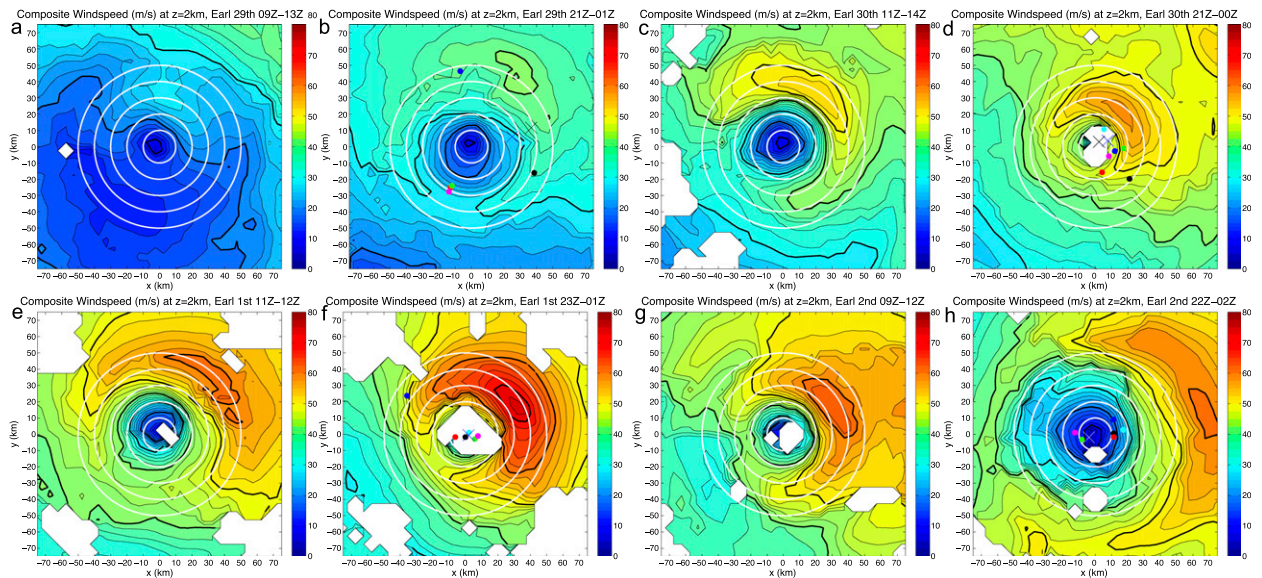


FIG. 2. Storm-centered horizontal cross sections of composite horizontal wind speed, for flights at approximately (a) 1100 UTC 29 Aug, (b) 2300 UTC 29 Aug, (c) 1200 UTC 30 Aug, (d) 2200 UTC 30 Aug, (e) 1200 UTC 1 Sep, (f) 0000 UTC 2 Sep, (g) 1100 UTC 2 Sep, and (h) 0000 UTC 3 Sep. Each panel is $150 \text{ km} \times 150 \text{ km}$, and range rings are drawn in white at 10-km intervals from 10 to 50 km. Wind speed is contoured every 2 m s^{-1} , with every 10 m s^{-1} contour thickened. For periods when there were DC-8 flights [(b), (d), (f), and (h)], the time-median storm-relative horizontal location of each inner-core sonde is indicated, with the markers corresponding to those of Figs. 4, 5, 9, and 10. Note that the DC-8 sondes were dropped from 0 to 7 h prior to the approximate central time of the P-3 legs used for the composite wind speed analysis.

hurricane-force winds at 2-km altitude confined to the northeast quadrant (Fig. 2a). From the azimuthal-mean tangential winds (Fig. 3a), the RMW was 95 km at 2-km height, sloping outwards to about 110 km at 8-km height. The low-level RMW contracted rapidly over the following

12 h during intensification to 85 kt, and at 2300 UTC (Fig. 3b) it was 45 km at 2-km height. The upper-level RMW did not contract as much, and the eyewall had an anomalously large outward slope of nearly 6:1; see Fig. 2a of Stern et al. (2014).

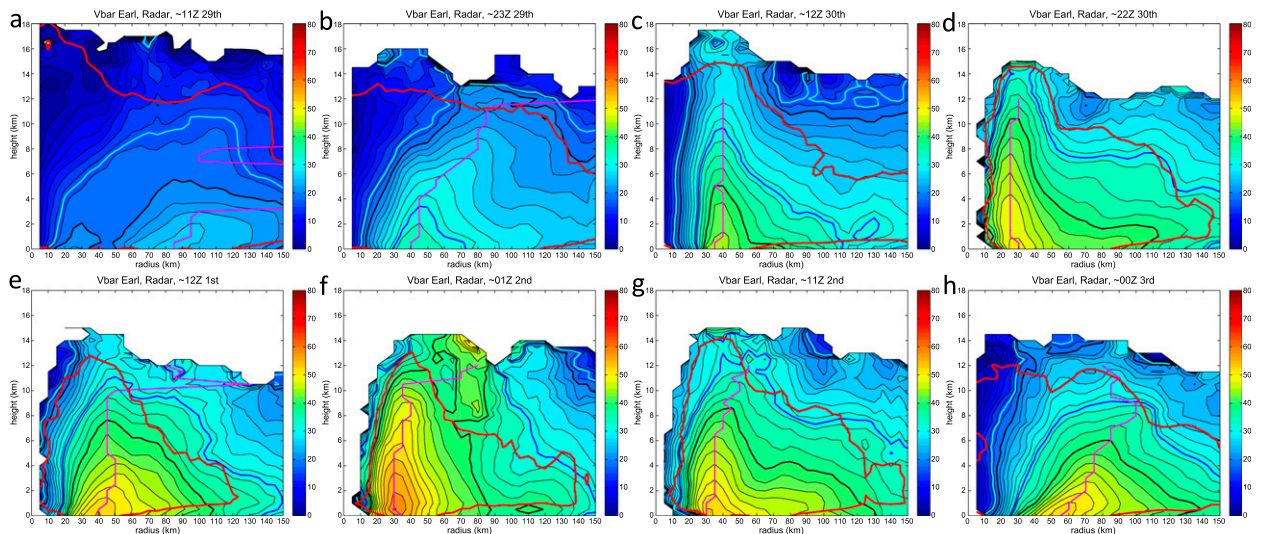


FIG. 3. For the same times shown in Fig. 2, radius-height plots of the azimuthal-mean tangential wind. Contours are every 2 m s^{-1} , with every 20 m s^{-1} in thick black. The 17 and 33 m s^{-1} contours are added, in cyan and blue, respectively. The RMW is plotted in magenta, from 0- to 12-km height. The red line is the 60% contour for data coverage: i.e., where 60% of grid points within the respective bin contain wind data.

As Earl continued to intensify to 105 and 115 kt for the flights at 1200 (Figs. 2c, 3c) and 2200 UTC (Figs. 2d, 3d) 30 August, respectively, the low-level RMW continued to contract (though more slowly than before) to 40 km and then 25 km. As the RMW contracted, its outward slope decreased, and the RMW was nearly vertical¹ between 2- and 10-km height. This decreasing outward slope with decreasing size is a general characteristic of tropical cyclones, as shown by Stern and Nolan (2009) and Stern et al. (2014).

A secondary wind maximum is evident at about 90–100 km in the northeast quadrant at 2200 UTC 30 August (Fig. 2d), as an ERC began. In the azimuthal mean (Fig. 3d) this is evident as a region with nearly constant tangential winds from 80–130-km radius. Likely as a consequence of the ERC, V_{\max} was constant at 115 kt through 1800 UTC 31 August and then weakened to 105 kt by 0600 UTC 1 September. Unfortunately, there was a 36-h gap in flights during this period. By the time of the next flight (1200 UTC 1 September), the ERC had completed, and a new larger eyewall was present, with a 45–50-km RMW from 2- to 8-km height (Fig. 3e). Despite being relatively large, the RMW had little outward slope. Following the ERC, Earl reintensified, with the low-level RMW contracting to 30 km as V_{\max} increased to 120 kt (Fig. 3f). Earl was still undergoing intensification during this flight, as peak intensity (125 kt) occurred 6 h later. Earl had begun to weaken rapidly by the next flight (1100 UTC 2 September), but V_{\max} was still 115 kt. Another ERC had begun, evident in the azimuthal mean as a broadening of the wind field (Fig. 3g), with a flat radial profile from 70 to 100 km. The ERC can also be seen in the horizontal cross section (Fig. 2g), but only in the northeast quadrant. By the time of the final flight that we examine (0000 UTC 3 September), V_{\max} had decreased to 90 kt, and a tremendous expansion of the wind field had taken place, with the RMW 70 km at 2-km height, sloping outwards to 100 km at 8-km height (Fig. 3h).

3. Analysis of the warm core

a. Inner-core dropsonde data

As part of NASA's GRIP field program [see Braun et al. (2013) for an overview], the DC-8 flew four

missions into Hurricane Earl on 29 and 30 August and 1 and 2 September. These missions span a range of intensities from category 1 to category 4 and include portions of both the RI and rapid weakening phases of Earl. Note that each DC-8 flight partially overlapped in time with a corresponding P-3 flight, although the two aircraft were not necessarily near the storm center at the same time. The DC-8 generally flew at altitudes of 11–12 km (250–200 mb), releasing 24, 23, 29, and 33 dropsondes on each respective day. The NCAR Earth Observing Laboratory (EOL) quality controlled and postprocessed these data using NCAR's Atmospheric Sounding Processing Environment (ASPEN) software. Starting from this dataset (Young et al. 2011), we first find all sondes that are within 50 km of the storm center.² There are 8 such sondes for each of the first two flights (29 and 30 August) and 7 for each of the latter two flights (1 and 2 September). Of these inner-core sondes, 0, 6, 6, and 7 were dropped within 15 km of the low-level center on each respective day. There were only a few sondes dropped very close to the low-level center, and this can potentially lead to an underestimation of the warm-core magnitude. Figures 4 and 5, respectively, show the vertical profiles of distance from the storm center and of wind speed for all of the sondes that were dropped within 50 km of the center. In the discussion that follows in section 3b, we will refer to individual sondes both by their drop time and by the order in which they were dropped (#1, #2, #3, etc.). Note that six of the dropsondes analyzed by Durden (2013) were from Earl, all of which we also include in this study.

While some sondes on each day sampled light winds at all heights (Fig. 5), it can be seen that a number of sondes sampled strong winds ($25\text{--}50\text{ m s}^{-1}$) at low levels, and these profiles are in part representative of the eyewall. This is particularly true on 29 August, when all eight sondes were dropped well inside of the flight-level RMW but near to the low-level RMW and therefore within the eyewall (cf. Figs. 3b and 4a). Note that the time-median storm-relative location of each sonde is also indicated on the composite horizontal cross sections of wind speed shown in Fig. 2. That none of the DC-8 sondes on 29 August were very close to the low-level storm center may be due in part to the fact that there was no eye apparent in visible satellite imagery until 1200 UTC 30 September (not shown). In the absence of a well-defined

¹ Given the 5-km grid spacing of the data, there may be a small outward slope to the RMW that cannot be resolved. Additionally, there is likely a substantial slope below 2-km height that is not apparent in the Doppler analysis as a result of known limitations in resolving the structure of the boundary layer.

² We use the storm centers that were estimated by HRD from the P-3 flight-level observations, based on the technique of Willoughby and Chelmon (1982). The time between these center locations is 2 min, and we interpolate the center to the time of the dropsonde.

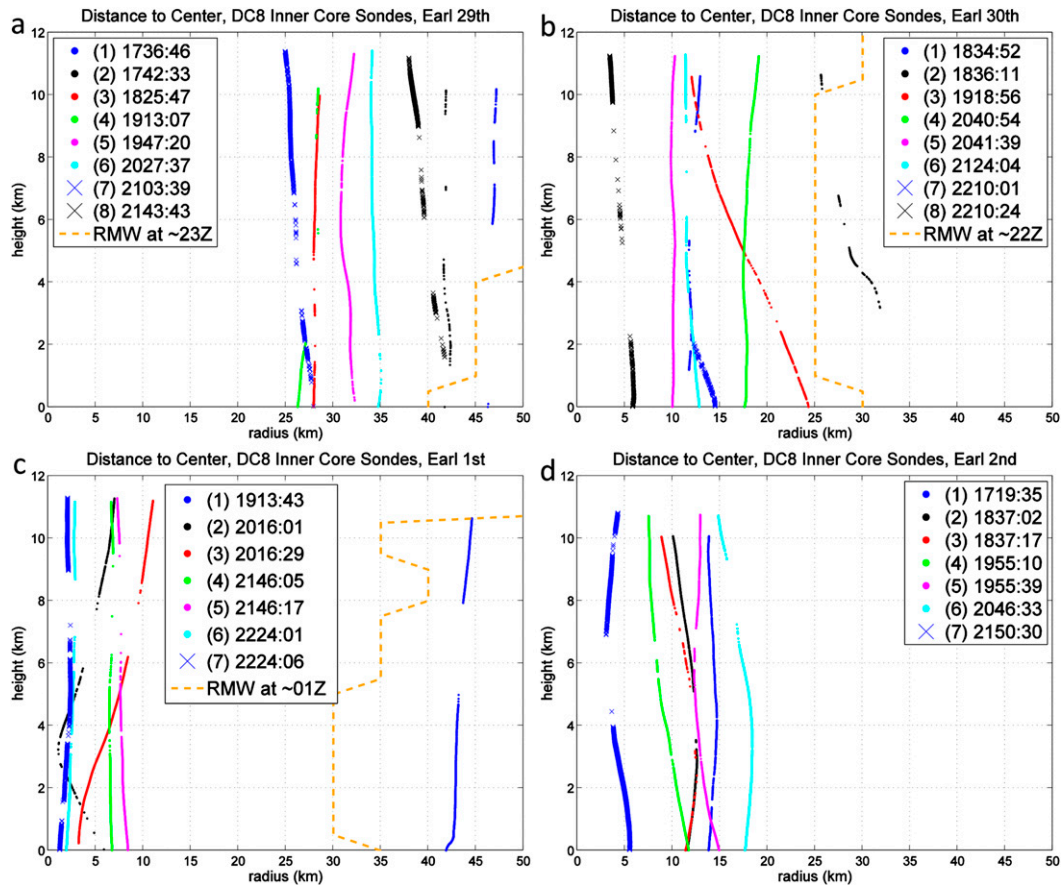


FIG. 4. For each of the DC-8 flights, vertical profiles of the distance of each inner-core sonde from the center: (a) 29 Aug, (b) 30 Aug, (c) 1 Sep, and (d) 2 Sep. The UTC times of the drops are given in the legends, with format hhmm:ss. Symbols correspond to those in Figs. 2, 5, 9, and 10. For (a), (b), and (c), the RMW from the corresponding time in Figs. 3b, 3d, and 3f, respectively, is plotted in dashed orange. For (d), the RMW lies outside of the range of the plot at all heights and is not shown.

eye, it can be challenging to direct a flight toward the storm center. Although the vortex was largely aligned vertically, Rogers et al. (2015) showed that there was a 10-km displacement between the centers at 2- and 7-km height at this time. Presumably, the tilt is even greater between 2- and 12-km height, and this also may have contributed to difficulties in dropping sondes near the low-level center. In any case, it is likely that the absence of sondes near the low-level center on 29 August leads to an underestimate in the magnitude of the warm core, particularly in the lowest 6 km. This, in turn, may affect the apparent height of the maximum perturbation temperature.

b. Warm-core structure

To calculate the perturbation temperature, it is first necessary to choose a reference state. SN12 provided a discussion of the various choices of reference profiles used in prior observational and numerical studies.

Halverson et al. (2006) used a DC-8 dropsonde 610 km to the southeast of Hurricane Erin to define the environmental sounding from the surface to 329 mb and an ER-2 dropsonde 340 km to the northeast of Erin to define the sounding above 329 mb. They stated that these two sondes were both very similar to each other below 350 mb and to the Jordan (1958) mean hurricane season sounding. In their AMSU satellite study, Knaff et al. (2004) defined the environment as the azimuthal-mean temperature in the 500–600-km annulus. Based in part on these two observational studies, SN12 chose the azimuthal mean from 550–650-km radius as the environment in their idealized simulations. Ultimately, any choice is somewhat arbitrary, though SN12 argued that, at least for numerical simulations, “some sort of average (at constant height) over an area at least several hundred kilometers away from the center is most appropriate” (p. 1679). Durden (2013) investigated the effect of using near-storm environmental soundings versus the

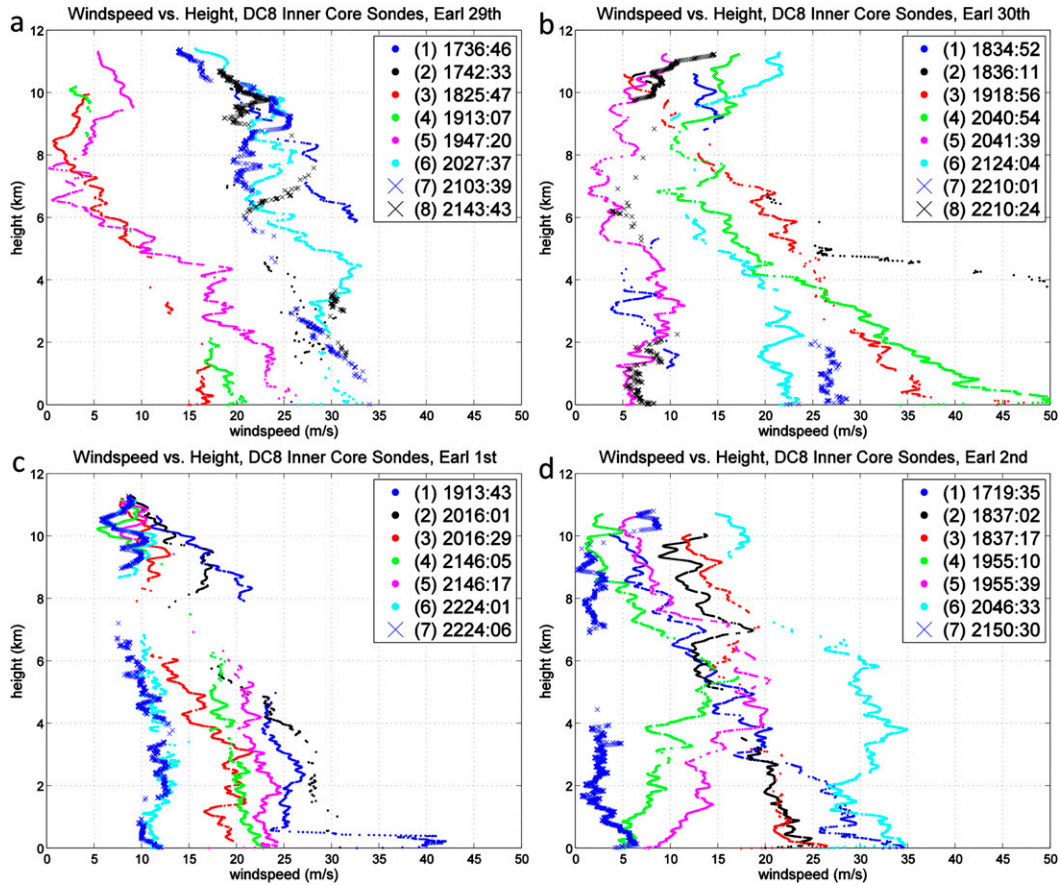


FIG. 5. As in Fig. 4, but for vertical profiles of wind speed.

climatological sounding of Dunion (2011).³ He found that, for most storms, the environmental soundings were warmer than the Dunion sounding and that, as a result, the perturbation temperature calculated using actual environmental soundings was usually cooler than that using the Dunion sounding. For some cases, the height of the maximum perturbation temperature was greater when using the Dunion sounding. This is consistent with what SN12 found as well.

In this study, we present results using both actual environmental soundings and the Dunion mean sounding. For environmental soundings, we use dropsondes released by the NOAA Gulfstream IV (G-IV) aircraft as part of “synoptic surveillance” missions. For each DC-8 flight, there was a G-IV flight at a similar time (the greatest separation was on 2 September, when the G-IV sondes were released 6–12 h prior to the DC-8 sondes),

releasing sondes from 12–14.5-km height and from 150–1000 km away from the storm center. The G-IV sondes were postprocessed and quality controlled by the first author using NCAR’s ASPEN software. A few sondes on each flight had mechanical problems or bad data and were removed from the final dataset, which contains 27, 31, 31, and 33 sondes on each respective day.

Figure 6 shows the temperature profiles from the G-IV sondes on each day, color-coded by their distance from the center. It can be seen that the temperatures generally increase inwards, consistent with Fig. 7 of Durden (2013), and as expected from thermal wind balance. There is also a fair amount of scatter evident among the profiles, with temperatures at any given height varying by 1°–6°C among dropsondes at similar distances from the center. This can be seen better in Fig. 7, which shows the perturbation temperature of each G-IV sounding relative to the Dunion sounding (i.e., at each height, we subtract the temperature of the Dunion profile from that of the G-IV sondes). Most G-IV soundings are warmer than the Dunion sounding at most heights, and this difference generally increases

³The Dunion (2011) “moist tropical” sounding has a nearly identical temperature profile to the Jordan (1958) hurricane season sounding.

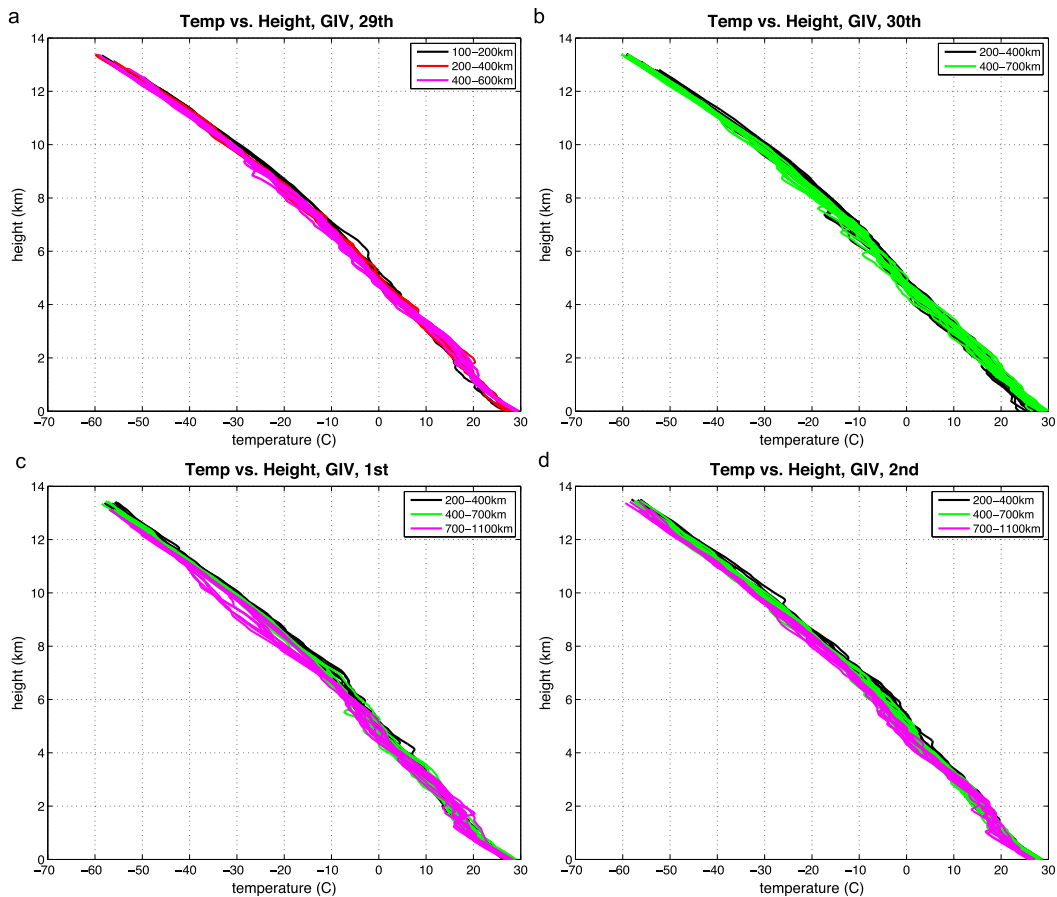


FIG. 6. Vertical profiles of temperature for all G-IV dropsondes: (a) 29 Aug, (b) 30 Aug, (c) 1 Sep, and (d) 2 Sep. The profiles are colored by distance of each sonde from the storm center, as indicated in each legend. Note that a given color does not correspond to the same range within each panel, and the range of distances is not identical among the panels.

with height, particularly above 6 km. In a number of soundings, there is a maximum in this perturbation temperature at about 12 km, whereas, in others, the maximum evidently occurs above the release height of the sonde.

It is clear that there will be a systematic difference in perturbation temperature for the DC-8 inner-core sondes when using reference profiles from environmental G-IV soundings and the Dunion sounding. Further, the variability among the G-IV profiles indicates that the magnitudes and detailed structure of the warm core would be sensitive to which individual G-IV sounding happens to be chosen to define the environment. Therefore, we choose not to use an arbitrary individual sounding as a reference profile and instead use a mean environmental profile. Figure 8 shows the mean G-IV profiles of perturbation temperature on each day, as well as the means within different radial bins. There is a consistent mean structure on each day, which is only

about a degree warmer than the Dunion sounding in the lowest 5 km, increasing above to about 4°C warmer at 12 km. There is also a local maximum at 2–3 km and a local minimum at 4–5 km on each day. Finally, it is evident that, while the mean temperature decreases with increasing radius above 4-km height, there is a reversed radial gradient below 4-km height on 29 and 30 August. This is consistent with the fact that the mean wind speed at 200–600-km radius actually increases with height to about 4 km on these days (not shown).

Figure 9 shows the perturbation temperature of the DC-8 inner-core sondes with respect to the Dunion sounding. As the reference profile here is the same at all times, changes in perturbation temperature with time correspond to changes in actual temperature. Strong warming at all heights is evident from 29 to 30 August (cf. Figs. 9a and 9b), consistent with the fact that Earl strengthened from 75 kt (978 mb) to 115 kt (938 mb) from 1800 UTC 29 August to 0000 UTC 31 August.

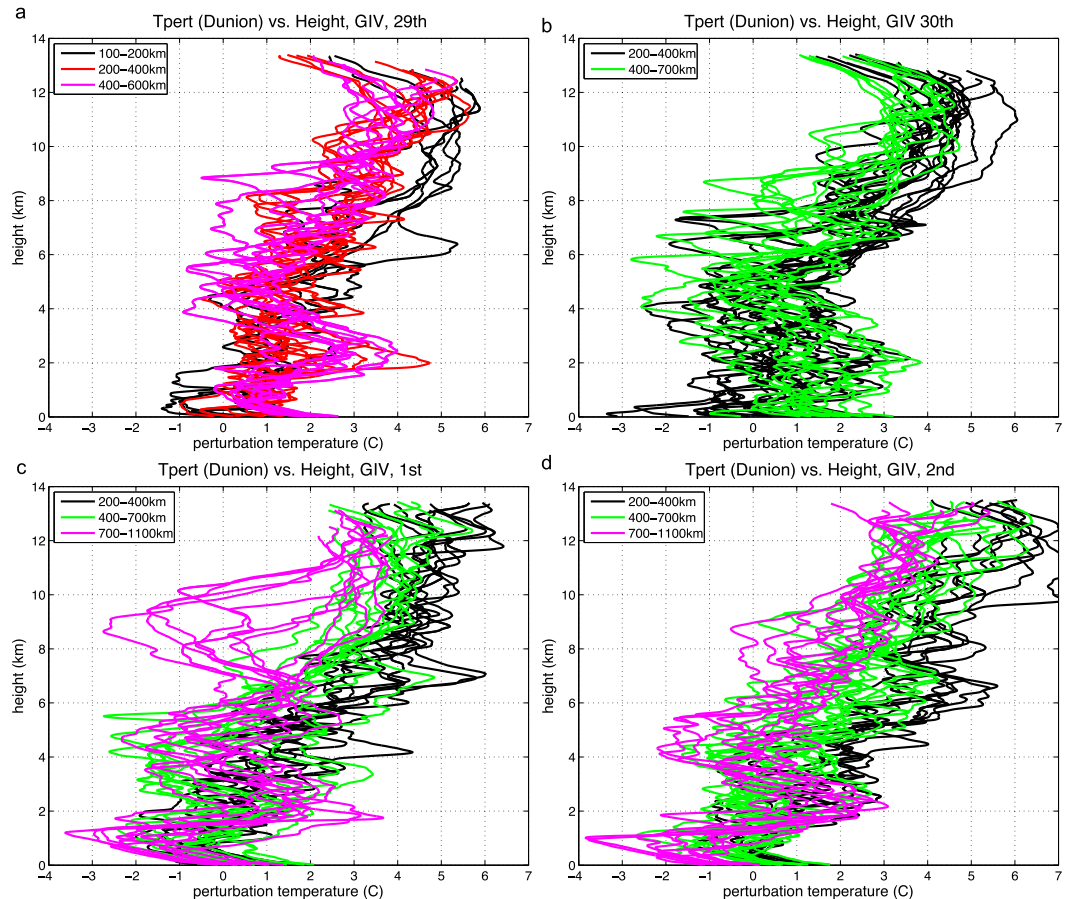


FIG. 7. As in Fig. 6, but for the perturbation temperature with respect to the Dunion sounding. Colors and distance ranges in each panel correspond to the analogous panels in Fig. 6.

Between the DC-8 flights on 30 August and 1 September (a 48-h period), there is further warming (cf. Figs. 9b and 9c), mostly above 6-km height. Despite weakening from 120 kt (932 mb) to 90 kt (949 mb) between 0000 UTC 2 September and 0000 UTC 3 September, the perturbation temperature profiles in Earl did not change substantially over this period (cf. Figs. 9c and 9d); in fact, there was warming between 4- and 8-km height. Given the increase in surface pressure, this implies that cooling likely occurred in a layer above 12 km (unsampled by the dropsondes).

It is apparent that the perturbation temperature profiles exhibit variability in the vertical on a number of scales. As a result, it is not trivial to determine what qualifies as a distinct local maximum in warm-core strength. For some sondes on 29 August, there is a distinct absolute maximum in perturbation temperature at 9 or 10 km, whereas for others the maximum is apparently above the sonde release height. There appear to be secondary maxima at 4 km in sonde #6 (2027:37 UTC), 6 km in #7 (2103:39 UTC), and 7 km in #8 (2143:43

UTC). Note that these three sondes were all dropped 25–40 km to the east of the center and therefore likely underestimate the magnitude of the warm core. On 30 August, only one sonde (#4, 2040:54 UTC) seems to have a clear absolute maximum in perturbation temperature, in this case at 9.5-km height. The other sondes all have perturbation temperatures increasing to the top of their profiles, although they do appear to become nearly constant at the top. Variability among the sondes is largest on 30 August, but this appears to largely be a result of several sondes sampling the eyewall (Figs. 2d, 4b, 5b). The RMW is smallest on this day, and so this variability therefore reflects the mean negative radial gradient in temperature. For example, at 4-km height, #5 (2041:39 UTC) is about 5°C warmer than #3 (1918:56 UTC). Although #3 (1918:56 UTC) is less than 10 km farther outward than #5 (2041:39 UTC) at this height, the wind speeds in #3 (1918:56 UTC) in the lower troposphere are 25–50 m s⁻¹. For the three sondes that are clearly within the eye (#1, 1834:52 UTC; #5, 2041:39 UTC; and #8, 2210:24 UTC) at all heights, there is

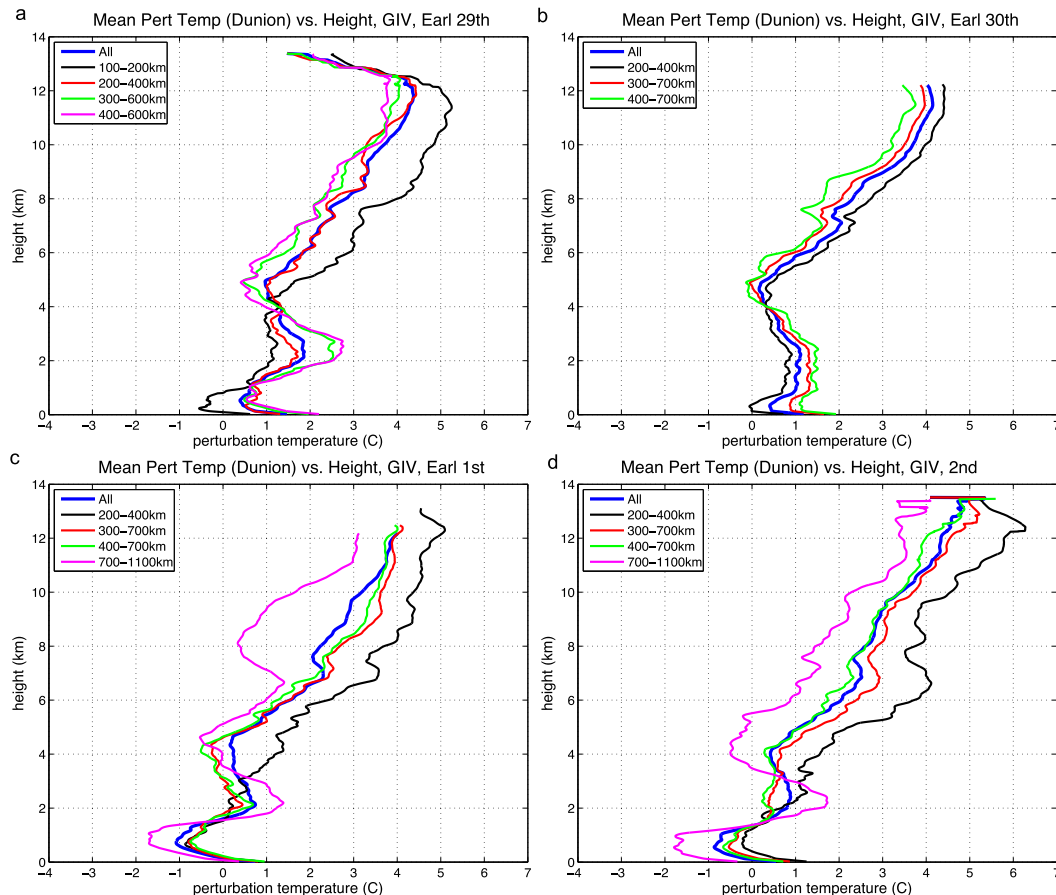


FIG. 8. As in Fig. 7, but for the mean perturbation temperature with respect to the Dunion sounding, binned by distance of the sondes from the storm center. Colors and distance ranges in each panel correspond to the analogous panels in Figs. 6 and 7, except that additional lines for the mean of all sondes and for the mean of sondes from 300 to 700 km have been added. Note that on 29 Aug no sondes were dropped beyond 600 km, so the ranges shown differ from the other days.

evidence of a secondary maximum in perturbation temperature at 4–5 km. On 1 September, some sondes seem to exhibit an absolute maximum in perturbation temperature at about 10-km height, while other profiles continue increasing to the top. Unlike on 30 August, none of the sondes on 1 September with low wind speeds have prominent secondary maxima in perturbation temperature. On 2 September, all of the sondes increase in perturbation temperature until the top of their profiles, except possibly #5 (1955:39 UTC), which has a maximum near 8 km. There is some evidence of secondary maxima at about 5-km height in #6 (2046:33 UTC) and #7 (2150:30 UTC).

Figure 10 is similar to Fig. 9, but using the mean profile of all G-IV sondes from 300 to 700 km from the center to define the reference state. We choose this radial range both for consistency with prior studies and consistency of data coverage between different days. Since the

vertical structure of temperature is qualitatively the same among the different bins shown in Fig. 8, we do not believe that the following results are that sensitive to the particular bin choice. Consistent with the implication of Fig. 8, using the G-IV profiles instead of the Dunion sounding as a reference results in cooler perturbation temperatures in the upper troposphere. On 29 August, the maxima at 9–10-km height become somewhat more distinct when using the G-IV reference profile instead of the Dunion profile. The secondary maximum in #7 (2103:39 UTC) that is evident at 6-km height using the Dunion reference profile becomes the absolute maximum using the G-IV sondes. On 30 August, distinct local maxima at 4–5-km height are evident in five profiles, and such maxima are substantially more pronounced than are the analogous midlevel local maxima evident in Fig. 9. In two of the three sondes with the weakest wind speeds

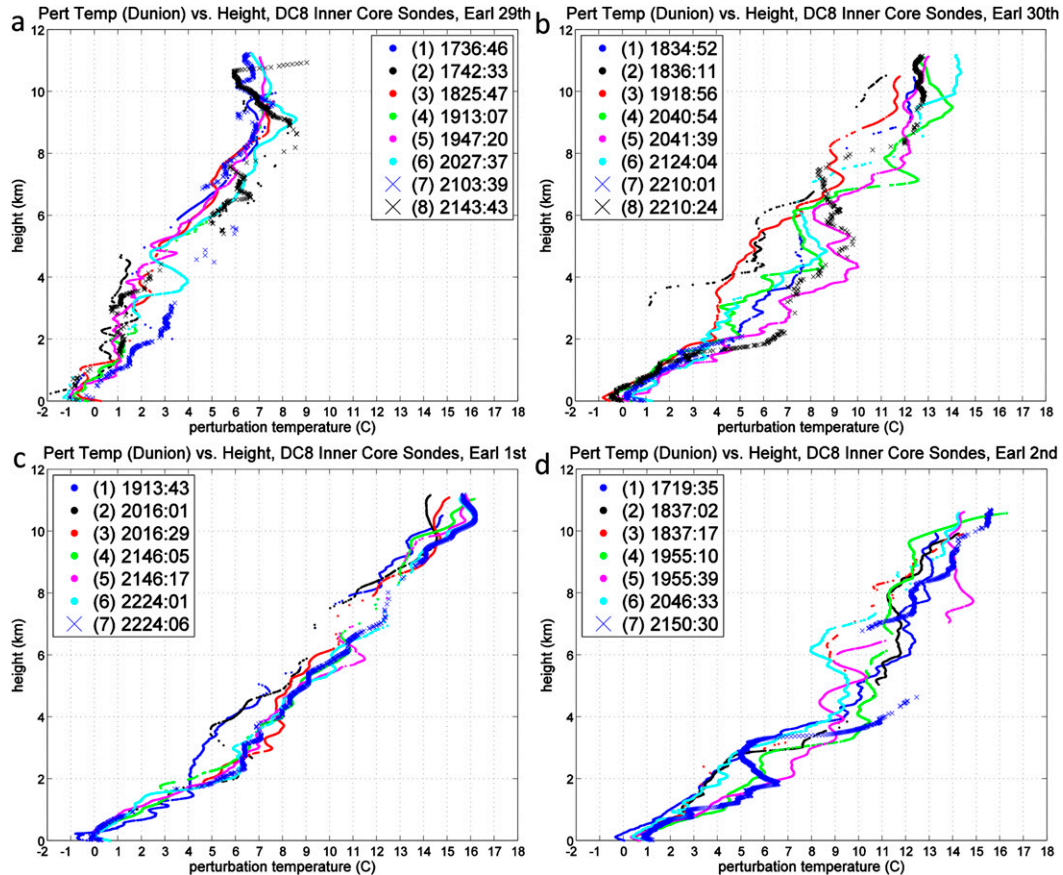


FIG. 9. For each of the DC-8 flights, vertical profiles of the perturbation temperature with respect to the Dunion sounding, for each inner-core dropsonde: (a) 29 Aug, (b) 30 Aug, (c) 1 Sep, and (d) 2 Sep. Note that since the reference sounding is identical for all flights/sondes, differences in perturbation temperature at a given height correspond to differences in actual temperature.

(#5, 2041:39 UTC and #8, 2210:24 UTC), these midlevel local maxima are nearly equal in magnitude to the absolute maxima, which are found at 8–9 km (when using the G-IV reference profile). On 1 September, the main effect of using the G-IV sondes as a reference profile is to decrease the rate at which perturbation temperature increases with height in the upper troposphere without altering the height where the maxima are found. On 2 September, several sondes now have mid-level maxima that are nearly equal in magnitude to the upper-level maxima, including #7 (2150:30 UTC), which is the sonde closest to the center.

It is clear that, for Hurricane Earl, the height of the absolute maximum perturbation temperature is quite sensitive to the chosen reference profile at times. The use of a local environmental reference state will tend to accentuate midlevel maxima in perturbation temperature, in comparison to using the Dunion profile as a reference. This is because the local environment of Earl is systematically warmer than the Dunion mean tropical

sounding, and this relative warmth increases with height. This explains why, on 30 August and 2 September (and to a lesser degree on 29 August), defining perturbation temperature using the local environment yields distinct mid- and upper-level maxima of approximately equal strength, whereas defining perturbation temperature using the Dunion profile yields upper-level maxima that are substantially stronger than any midlevel secondary maxima. As discussed in SN12, the sensitivity of the height of the maximum warm core to the reference profile is complicated, as it depends on both the vertical profile of the difference between the two reference states and the vertical profile of the inner-core temperature itself. Therefore, it is not surprising that there are times, such as on 1 September for Earl, where the height of the maximum perturbation is insensitive to the reference profile. As Fig. 8 indicates, the warmth of the environment relative to the Dunion mean sounding does not change much between 30 August and 1 September. This suggests that it is the vertical profile of the inner-core

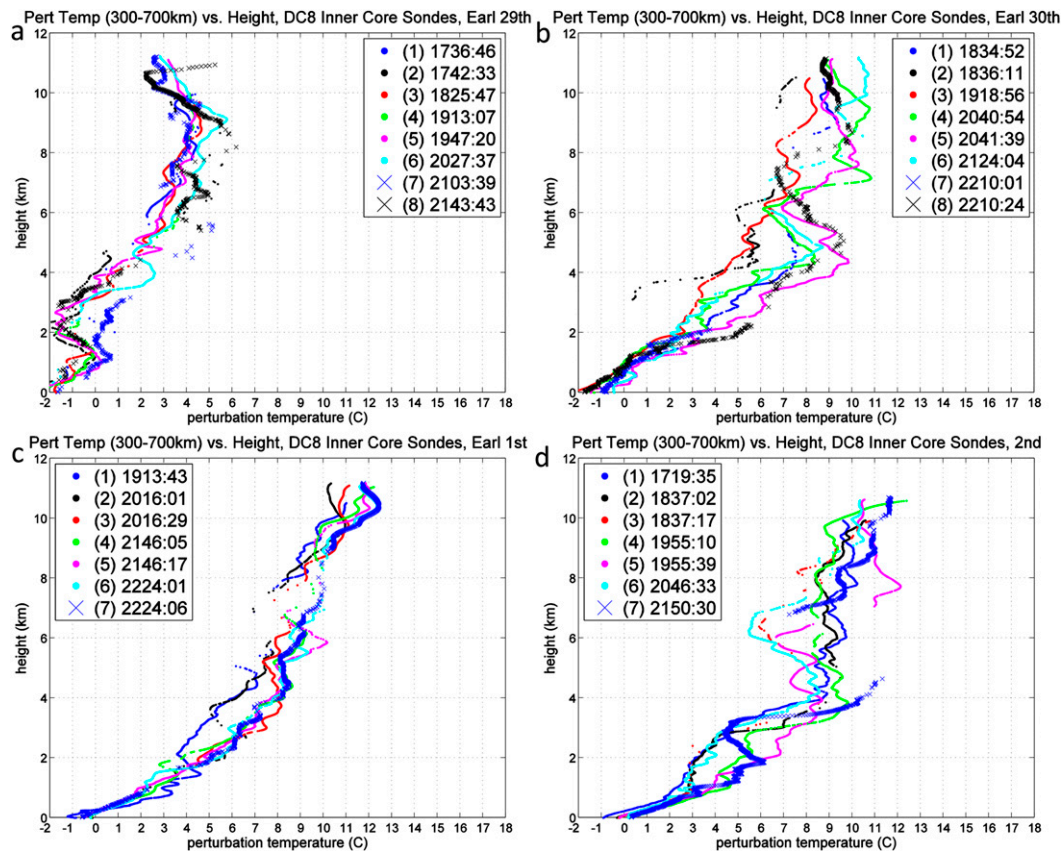


FIG. 10. As in Fig. 9, but with perturbation temperature defined with respect to the mean temperature of all G-IV dro sondes within 300–700-km distance from the storm center. For each DC-8 flight, the sondes that define the reference profile are taken from the G-IV flight that is closest in time. This reference profile is identical for all sondes dropped within the same flight but differs for each flight.

temperature that renders the height of the warm core insensitive to the reference state on 1 September.

Although the height of the absolute maximum perturbation temperature in Earl varies with time, as does the existence of multiple distinct maxima, there does not seem to be an obvious systematic pattern to this variation. Using the G-IV reference profile, the strongest and most well-defined midlevel maxima in perturbation temperature occurred on 30 August and 2 September. During the flight on 30 August, Earl was at the end of a period of RI, while on 2 September Earl was rapidly weakening. The flight with the strongest signature of a single upper-level maximum was on 1 September, which occurred during another period of intensification. The intensity of Earl was nearly the same during the flights on 30 August and 1 September, yet they have noticeably different vertical profiles of perturbation temperature. From the observations alone, there is little evidence that there is a relationship between the height of the warm-core maximum and intensity or intensity change. Despite Earl being one of the most well-sampled tropical

cyclones yet observed, it is still quite difficult to draw conclusions regarding the time evolution of the warm core. In the following section, we examine a numerical simulation of Earl in order to gain further insight.

4. WRF simulation of Earl

a. Model configuration

To simulate Earl, we use the 2013 configuration of The Pennsylvania State University (PSU) Real-Time Weather Research and Forecasting Ensemble Kalman Filter (WRF-EnKF) system (note that this is a retrospective forecast). We use the Advanced Research WRF (WRF-ARW), version 3.4.1, with 3 nested domains (27-/9-/3-km horizontal grid spacing) and 43 vertical levels. To parameterize unresolved physical processes, we use the Yonsei University (YSU) boundary layer parameterization, the WSM6 microphysics scheme, and the RRTM and Dudhia parameterizations for longwave and shortwave radiation, respectively. The surface exchange coefficients of heat and momentum

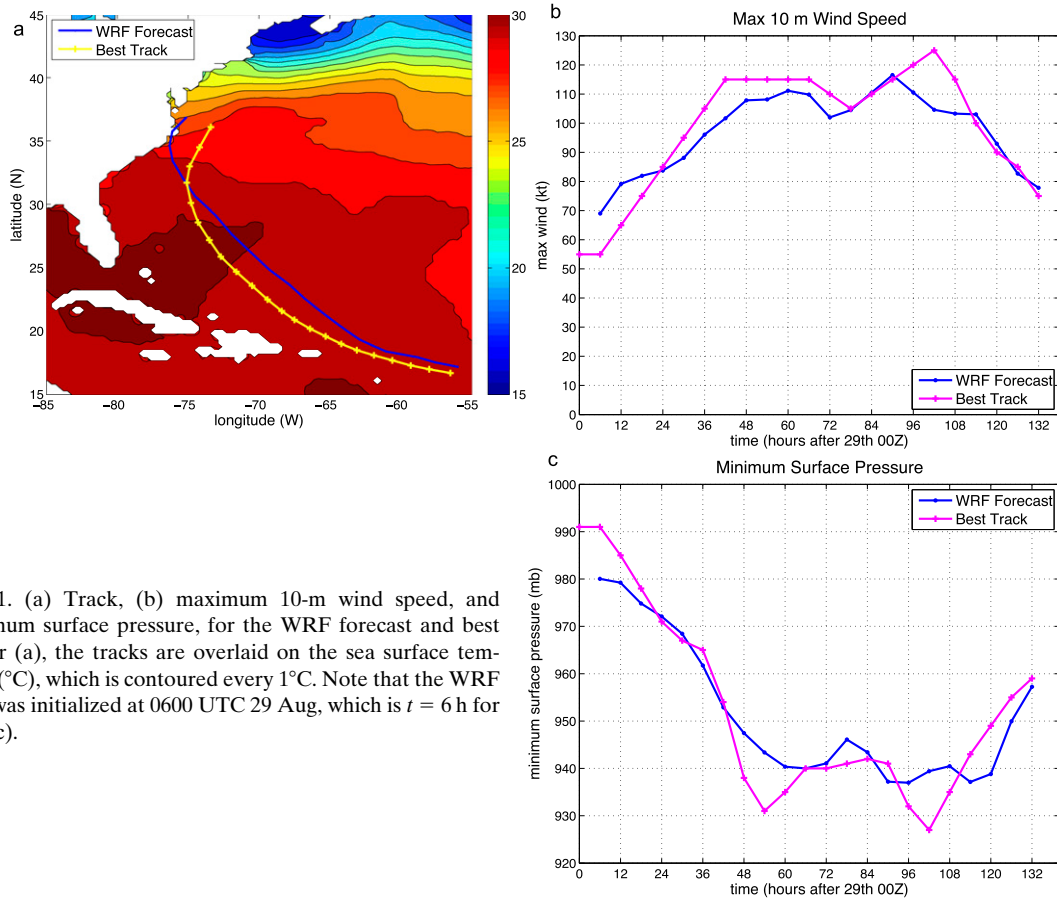


FIG. 11. (a) Track, (b) maximum 10-m wind speed, and (c) minimum surface pressure, for the WRF forecast and best track. For (a), the tracks are overlaid on the sea surface temperature ($^{\circ}\text{C}$), which is contoured every 1°C . Note that the WRF forecast was initialized at 0600 UTC 29 Aug, which is $t = 6$ h for (b) and (c).

are as in the PSU formulation of Green and Zhang (2013). In this study, we examine a single deterministic simulation, which was initialized from the mean of a 60-member ensemble Kalman filter (EnKF) analysis. For this analysis, conventional Meteorological Assimilation Data Ingest System (MADIS) observations were assimilated, as were minimum surface pressure (P_{min} ; from NHC advisories), flight-level observations, and dropsondes. Data from the NOAA P-3 and G-IV aircraft were assimilated, but data from the DC-8 were not. Doppler radar observations were not assimilated for the simulation we examine. Further details on the EnKF assimilation system can be found in Weng and Zhang (2012) and Zhang and Weng (2015).

Deterministic forecasts were initialized every 6 h throughout the lifetime of Earl. After examining a number of different initialization times, we chose to focus on a single simulation, which was initialized at 0600 UTC 29 August and integrated until 1200 UTC 3 September. We chose this particular simulation because it was initialized prior to the first DC-8 flight and because it yielded a relatively accurate prediction of track, V_{max} , and P_{min} . While this forecast and some forecasts

initialized at other times produced relatively good predictions, others were less accurate. It is not the purpose of this study to assess intensity forecast skill or to examine the reasons for producing good versus poor forecasts. Instead, we seek a forecast that produces a relatively accurate simulation of Earl and then use it to examine the evolution of the warm-core structure, in comparison to observations. If the intensity forecast had large errors (in particular in P_{min}), then the vertically integrated temperature perturbation would be highly erroneous, and it would not be useful to compare the warm-core structure to observations. Therefore, we pick one of the better forecasts for our analysis and comparisons.

b. Comparison of forecast wind field to observations

Figure 11 compares the forecast position and intensity of Earl to the NHC best track. Earl's track is relatively well forecast (Fig. 11a), but with a slightly right-of-track bias at most times. Both V_{max} (Fig. 11b) and P_{min} (Fig. 11c) are also well forecast, with the peak intensity slightly underestimated and the forecast intensity tendency generally following that of the best track. Importantly for our analysis of the warm core, the forecast

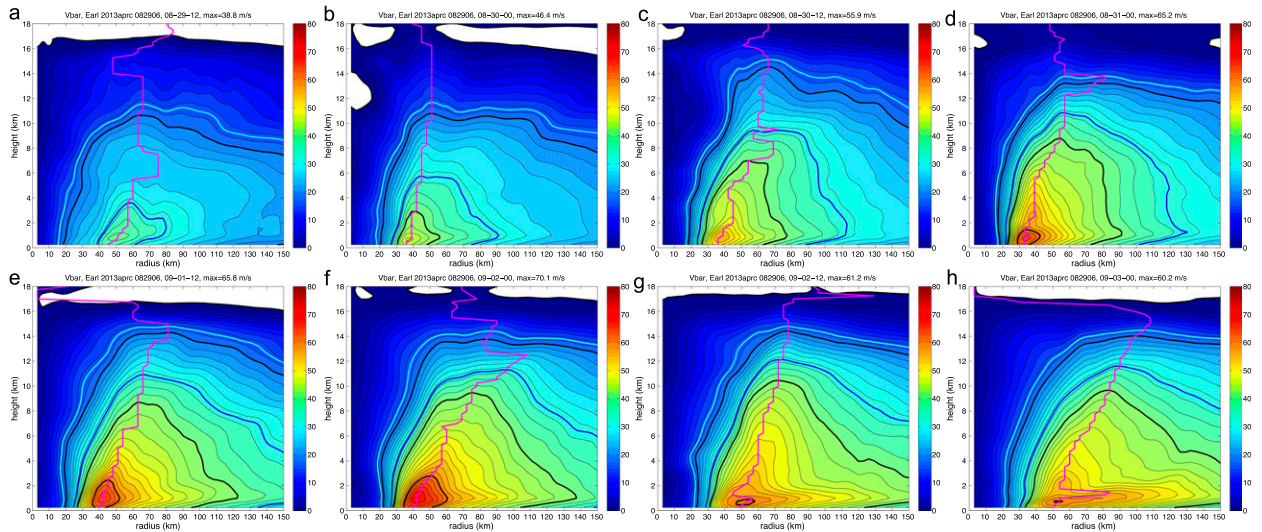


FIG. 12. As in Fig. 3, but for the WRF forecast. WRF output data were available at 6-h intervals, so each panel corresponds to the closest available time to the respective radar data.

P_{min} is within 10 mb of the best track at all times for which we have observations of the warm-core structure.

Before we compare the simulated warm-core structure to observations, we will first evaluate the forecast structure of the wind field. This is useful for two reasons. First, the radius–height structure of the perturbation temperature is closely related to the structure of the tangential winds through thermal wind balance. As discussed in SN12, this relationship is complicated, as, for example, the temperature at the storm center depends on the winds at all radii, and the radial temperature gradient at a given location is a function of radius, the vertical gradient of the winds, and the magnitude of the wind speed itself. Nevertheless, errors and biases in the structure of the temperature and wind fields are fundamentally linked, and it is possible to deduce errors in one field from errors in the other. Below, we will show that errors in the forecast warm-core structure of Earl are likely related to the fact that the RMW in the simulation tends to have too large of an outward slope. It is also useful to investigate the forecast structure of the wind field because simple intensity metrics, such as V_{max} and P_{min} , though important, are inherently limited in their utility and in the information they convey. For example, if a simulation accurately forecast V_{max} , but the RMW was twice as large as observed, this would constitute a serious error and would imply that the forecast V_{max} was correct for the wrong reason. Only recently have studies begun to focus on structural predictions, so this Earl dataset presents an opportunity to increase our understanding of model forecasts of structure.

Figure 12 shows the WRF forecast azimuthal-mean tangential winds at times corresponding (to the nearest 6 h) to the radar analyses shown in Fig. 3. Note that it is difficult to directly compare the peak azimuthal-mean tangential wind \bar{V}_{max} between the simulations and radar analyses. This is because \bar{V}_{max} in TCs is generally found within the boundary layer (typically 500–1000 m). Because of a combination of limited vertical resolution and the inherent smoothing of the variational analysis, the wind speeds in the upper part of the boundary layer in the radar analyses are almost certainly biased low. Therefore, our comparison is instead focused at 2-km height, which is representative of low levels but above the poorly resolved boundary layer. Compared to the radar analysis near 1200 UTC 29 August (Fig. 3a), the simulated Earl (Fig. 12a) is both too strong and substantially too small, with the low-level RMW nearly 40 km smaller than observed. By 0000 UTC 30 August (Fig. 3b), the radar analyses indicate that Earl contracted substantially, with the RMW at 2-km height decreasing from about 95 to 45 km. The simulated Earl contracted as well (Fig. 12b), and despite being much too small 12 h earlier, has a low-level RMW that is only about 5 km smaller than the observations at this time, a difference that is likely smaller than the analysis uncertainty. The observed RMW has a large outward slope above 4-km height, whereas the simulated Earl has a much more vertical eyewall and, consequently, an upper-level RMW that is still too small. Note that, at this time, the forecast V_{max} (Fig. 11b) and P_{min} (Fig. 11c) are almost identical to those of the best track. This demonstrates an example of how a good forecast of a

single measure of intensity does not necessarily indicate a similarly good forecast of storm structure. As discussed in SN12, the structure of the warm core is a complicated function of the wind field at all radii/heights, so subtle changes in the structure of the wind field can sometimes translate into large variations in the vertical structure of the warm core through thermal wind balance.

Between 0000 and 1200 UTC 30 August, the observed RMW becomes nearly vertical (Fig. 3c), while in contrast, the RMW in the simulation becomes more outwardly sloped (Fig. 12c). For most of the remainder of the simulation, the RMW has too great of an outward slope, and the upper-level RMW is too large. Stern (2010) found that, in idealized WRF simulations, the slope of the RMW was systematically too large as compared to the observational dataset of Stern and Nolan (2009). Such a bias in RMW slope was also found by Nolan et al. (2009) for their simulation of Hurricane Isabel (2005) and by Nolan et al. (2013) in a comparison of their nature run simulation to the observations of Stern et al. (2014). From 122 HWRF forecasts of four different hurricanes, Zhang et al. (2015) found that the RMW slope was systematically too large, for a given value of low-level RMW. On the other hand, Zhang and Marks (2015) found that, in their idealized HWRF simulations, the RMW slope compared well to observations. The study of Zhang and Marks (2015) notwithstanding, it seems clear that an RMW with too great of an outward slope is a common issue in numerical simulations of tropical cyclones, and one for which the cause is currently unknown.

As noted in section 2, Earl underwent an ERC between 0000 UTC 31 August (Fig. 3d) and 1200 UTC 1 September (Fig. 3e), and, as a consequence, the low-level RMW expanded from 25 to 45 km. Despite the absence of an ERC in the simulation (Fig. 12e), the RMW in the simulation also expanded to about 45 km at low levels during this time. Over the following 12 h, the observed RMW contracts again while the storm reintensifies (Fig. 3f). While this reintensification does occur in the simulated Earl (Fig. 12f), it is somewhat too weak, the peak occurs too early, and the simulation does not capture the observed RMW contraction. Another ERC begins in the observed Earl at 0000 UTC 2 September (Figs. 2f, 3f), and, in contrast to the first ERC, this later ERC is relatively well predicted in the simulation. Although the ERC starts about 12 h too late in the simulation (Fig. 12g), the initial radius of the secondary wind maximum is the same (110–130 km), and the evolution of the wind field is qualitatively consistent with the radar analyses. This radial expansion of Earl's wind field, which roughly coincides with the start of

recurvature (Fig. 11a), appears to be highly predictable, in contrast to the earlier ERC late on 30 August. Such an expansion is evident in numerous simulations we have examined at various lead times (not shown), including those for which intensity forecasts were poor. We therefore speculate that the large-scale environment is somehow responsible for this expansion, though further investigation is beyond the scope of this study.

c. Simulated warm-core structure

Figures 13 and 14 show the radius–height structure of the simulated perturbation temperature. To investigate the sensitivity of the warm-core structure to environmental reference state, we perform calculations using both the Dunion sounding (Fig. 13) and the mean environmental temperature (Fig. 14; from $r = 300$ to 700 km). The magnitude of the warm-core maximum is less when using the local environment as a reference, as is the case with observations. This is because the local environment (both simulated and observed) is systematically warmer than the Dunion profile. As in the observations, there is also a sensitivity of the height of the absolute maximum to the reference profile. Though the details of the sensitivity differ, the height of the maximum simulated perturbation temperature tends to be lower when using the local environmental reference profile, similar to the observations.

To best compare the simulations to the observed dropsondes, Fig. 15 compares dropsonde profiles of perturbation temperature in the eye with simulated vertical profiles at the model times and radii closest to observed. Figure 15a compares the observations to the simulation using the local environmental reference profile, while Fig. 15b uses the Dunion profile. In the following discussion, we focus on the comparison using the environmental reference. On 29 August, using the environmental reference (Fig. 15a), the shape of the simulated profile of perturbation temperature is quite similar to that observed, with both exhibiting broad maxima from 7- to 10-km height and both having the largest increase with height between 3 and 7 km. The simulated profile is 1°–2°C too warm at all heights above 2 km, consistent with the fact that the simulated Pmin is slightly too low. Note that the most representative “eye” sonde on 29 August is actually 30–35 km from the storm center, as no sondes were dropped close to the low-level center. Therefore, we examine the vertical profile in the simulation at $r = 33$ km; sampling at the simulated center would bias the comparison by 1°–2°C. Based on the radius–height structure of simulated perturbation temperature at this time, we speculate that if there had been a sonde dropped directly over the low-level center, the height of the maximum may have been a few

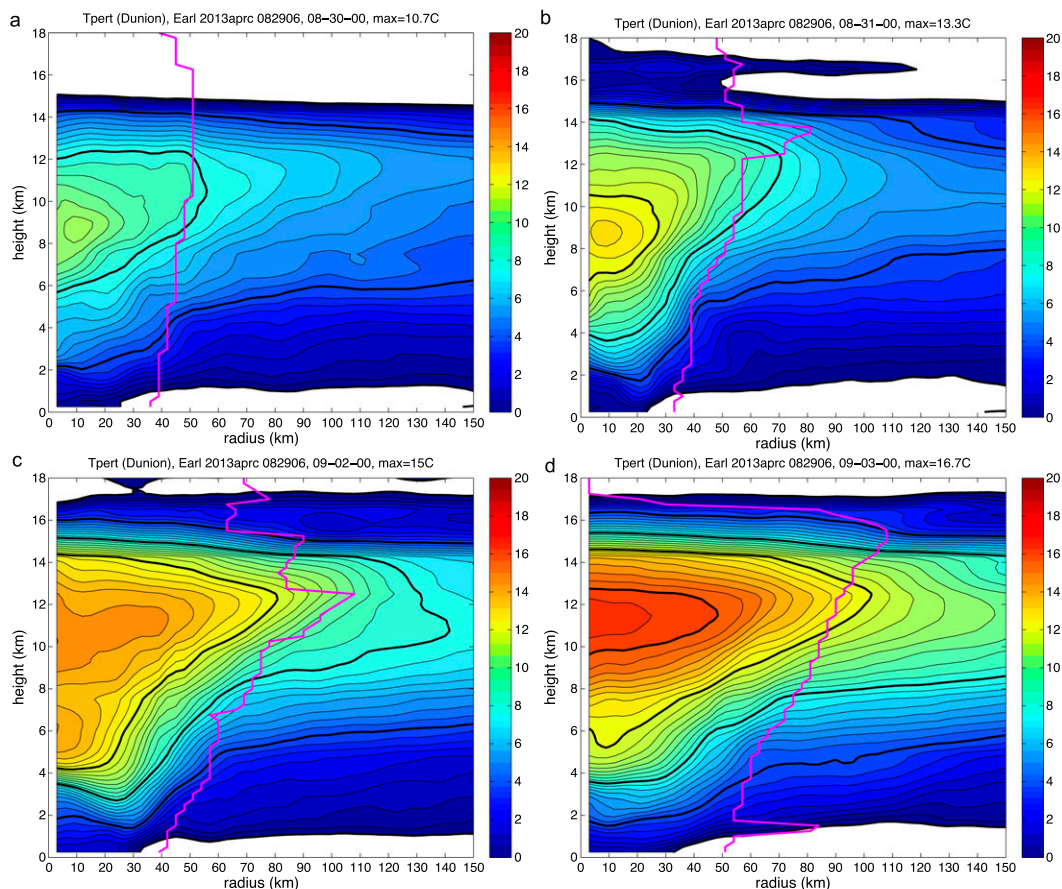


FIG. 13. For the WRF forecast, radius–height cross section of azimuthal-mean perturbation temperature, using the Dunion reference profile. Perturbation temperature is contoured every 0.5°C , with every 4°C thickened. White regions represent negative values. The forecast RMW is in magenta. Times shown are those that are closest to the respective DC-8 flights: 0000 UTC (a) 30 Aug, (b) 31 Aug, (c) 2 Sep, and (d) 3 Sep.

kilometers lower than seen in the observed sonde at 30-km radius.

Overall, the simulated vertical profile of perturbation temperature on 30 August is quite similar to the analogous observed profile. Both the pattern and magnitude of the simulated profile are similar to observations, but the simulated midlevel (4–5-km height) maximum is not quite as strong as observed, and the simulated perturbation temperature is too cold above 10-km height. At 1800 UTC 30 August, the simulated Pmin is nearly the same as the best track, while, at 0000 UTC 31 August, the simulated Pmin is about 10 mb too weak. This is consistent with the simulated perturbation temperature being comparable to observed but slightly too cool at some heights. Note also that, through thermal wind balance, the fact that the simulated temperature is too cool at upper levels is qualitatively consistent with the fact that the simulated winds at upper levels are too weak and that the upper-level RMW is too large.

Following the observed ERC and recontraction of the RMW (both of which are absent in the simulation), there are larger structural differences in the wind field between the observations and the simulation, with the mid- and upper-level RMW being much too large in the simulation. Therefore, it is not surprising that greater differences exist in the vertical profile of perturbation temperature at this time (1 September), as compared to previously. Neglecting small-scale details, the observed perturbation temperature increases monotonically with height to about 10.5 km, while simulated perturbation temperature has a distinct absolute maximum at about 5.5 km. The simulated profile is also 2° – 4°C warmer than observed from 4–7 km. As the simulated Pmin is slightly too weak at this time, this implies that the simulated perturbation temperature must be too cool at heights above those observed (i.e., above 11 km). Once again, this is consistent (through thermal wind balance) with the fact that the upper-level RMW is too large. Note

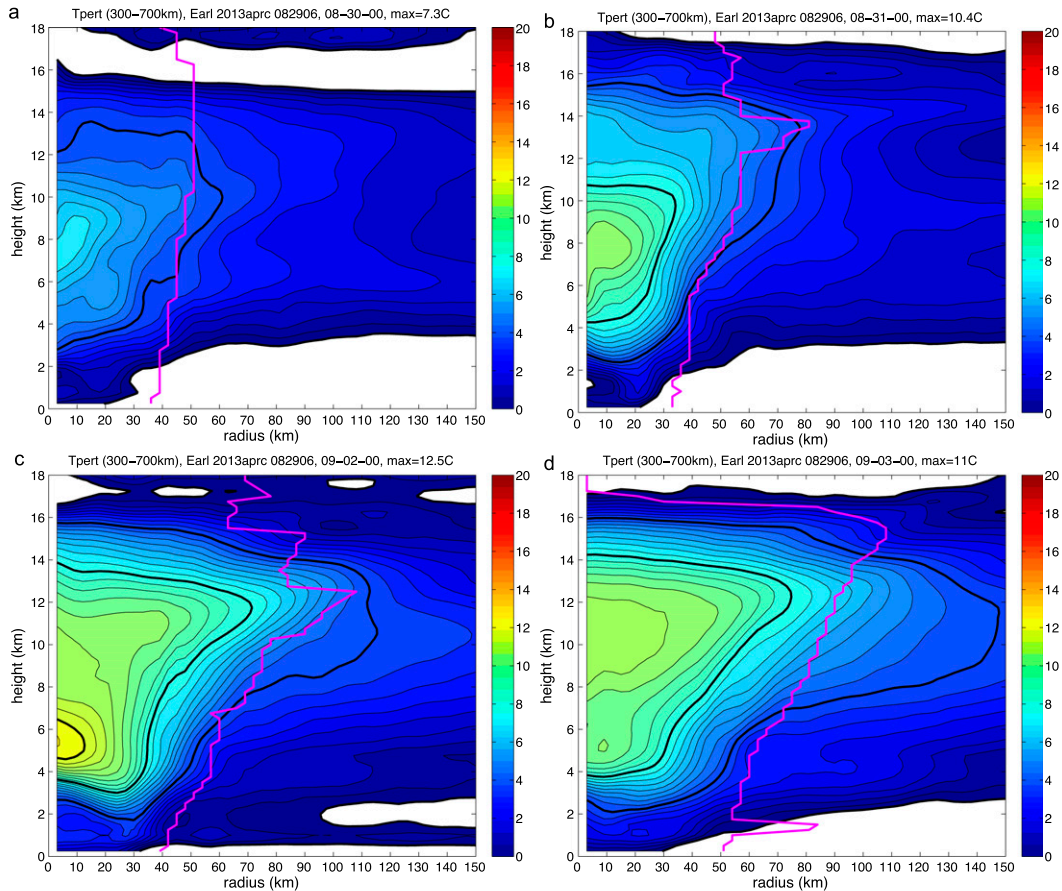


FIG. 14. As in Fig. 13, but using the azimuthal-mean temperature averaged between 300- and 700-km radius as the reference profile.

that, when using the Dunion reference state (Fig. 15b), the difference between simulated and observed perturbation temperature at midlevels is a few degrees larger than when using the environmental reference state (Fig. 15a); this implies that the simulated environment must be too warm at midlevels at this time (not shown).

For the last DC-8 flight (late on 2 September), there are again some differences between simulated and observed perturbation temperature profiles, although the agreement is better than on the previous day. Below 3 km, the simulated perturbation temperature is too cold, although this is partly due to the simulated environmental temperature being slightly too warm (not shown). There is a gap in the observations between 5 and 7 km, but it can be inferred that the simulation switches from being too cold to too warm across this layer. It can also be inferred that there is a midlevel local maximum in perturbation temperature in the observed profile. This maximum is missing from the simulation, which instead is characterized by a nearly constant profile from 5- to 12-km height. Nevertheless, overall, the warm-core

structure at this time is simulated rather well, considering that this is 4–5 days after initialization.

d. The relationship between changes in the temperature and wind fields

To illustrate the difficulty in relating specific structural changes in the warm core structure to changes in the wind field, in Fig. 16, we more closely examine the simulated evolution of both fields from 0000 UTC 2 September to 0000 UTC 3 September. During this 24-h period, the warm-core maximum in the simulation increases in height from 5.5 (Fig. 14c) to 9.5 km (Fig. 14d). From the 24-h temperature change (Fig. 16a), it is evident that the upward shift in the maximum is a result of slight cooling (1° – 2° C) of the eye from 2–8-km height, along with slight warming (1° – 2° C) above 8 km. Changes in the wind field are not directly related to these temperature changes, but instead to changes in the radial gradient of temperature $\partial T/\partial r$. Figures 16b and 16c show $\partial T/\partial r$ at 0000 UTC 2 and 3 September, respectively, and Fig. 16d shows their difference. Note that at neither time

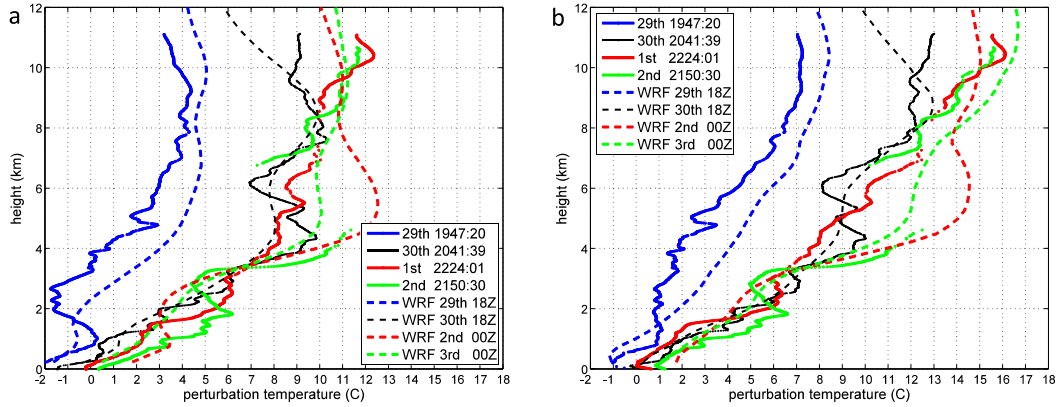


FIG. 15. For each DC-8 flight, the vertical profile of perturbation temperature for a representative inner-core sonde is compared to the WRF forecast at the closest available time. (a) Using the mean 300–700-km temperature as a reference profile and (b) using the Dunion sounding as a reference profile. Dropsondes are solid, and WRF soundings are dashed, with the times given in the legends. For WRF, the azimuthal mean is shown, at a radius corresponding to that of the respective observed sounding.

does the height of minimum $\partial T/\partial r$ correspond to the warm-core maximum, and the change in perturbation temperature seen between Figs. 14c and 14d cannot be easily inferred by looking at $\partial T/\partial r$. The structure of the 24-h change in $\partial T/\partial r$ is complex, but, in the region of strongest cooling, the negative temperature gradient generally weakens (positive tendency). As discussed in SN12, thermal wind balance does not simply relate $\partial T/\partial r$ to $\partial v/\partial r$, as is sometimes assumed. Starting from thermal wind balance in log–pressure height coordinates (Schubert et al. 2007),

$$\left(f + \frac{2v_g}{r}\right) \frac{\partial v_g}{\partial z} = \frac{g}{T_0} \frac{\partial T_v}{\partial r}, \quad (1)$$

approximating virtual temperature T_v with temperature T and neglecting the Coriolis parameter f ,

$$\frac{\partial T}{\partial r} = \frac{2T_0}{g} \frac{v_g}{r} \frac{\partial v_g}{\partial z}, \quad (2)$$

where v_g is the gradient wind and T_0 is a constant reference temperature. Figure 16e shows the 24-h change

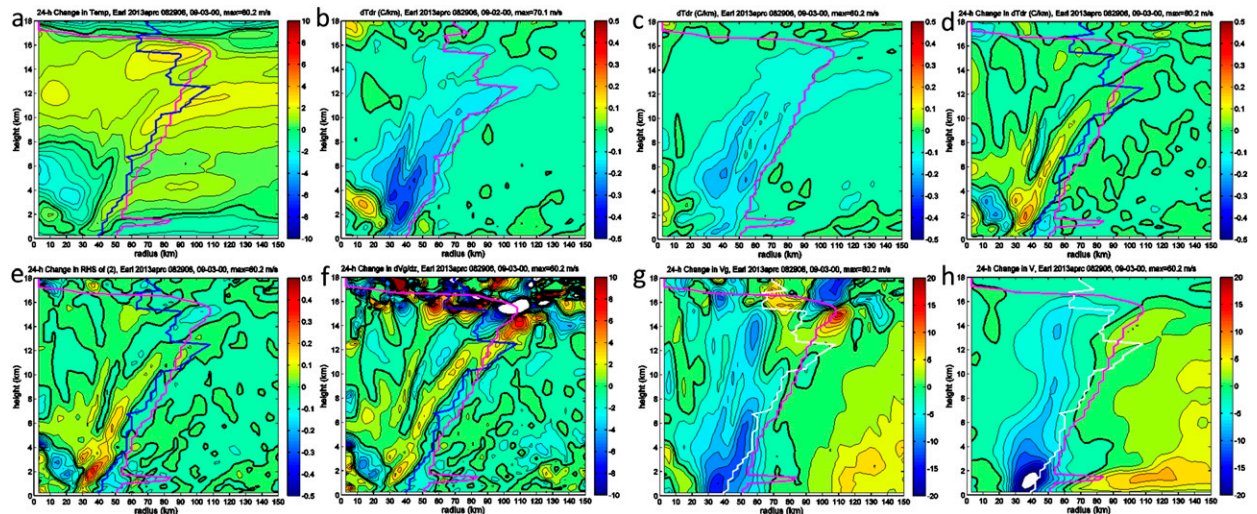


FIG. 16. For the WRF simulation, (a) 24-h change in temperature from 0000 UTC 2 Sep to 0000 UTC 3 Sep; $\partial T/\partial r$ ($^{\circ}\text{C km}^{-1}$) at (b) 0000 UTC 2 Sep and (c) 0000 UTC 3 Sep; and 24-h changes in (d) $\partial T/\partial r$, (e) the rhs of (2), (f) $\partial v_g/\partial z$, (g) V_g , and (h) V . The contour intervals are 0.5°C in (a), $0.05^{\circ}\text{C km}^{-1}$ in (b)–(e), $1\text{ m s}^{-1}\text{ km}^{-1}$ in (f), and 2 m s^{-1} in (g)–(h). The RMW at the current time is shown in magenta in (b) and (c), the RMW at 0000 UTC 2 and 3 Sep are shown in blue and magenta, respectively, for (a) and (d)–(f), and in white and magenta, respectively, for (g) and (h). The zero contour is in thick black on all panels.

in the rhs of (2), using $T_0 = 300$ K. Comparing Figs. 16d and 16e, it is evident that (2) is an excellent approximation to exact thermal wind balance.

From Fig. 16e, it remains difficult to comprehend the relationship between the changes in warm-core structure and the wind field. Figure 16f shows the 24-h change in $\partial v_g / \partial z$, which, in this particular case, qualitatively resembles the change in the full rhs of (2). Here, we can see that the weakened radial temperature gradient approximately corresponds to a region of weakened vertical gradient of v_g . Figure 16g shows the 24-h change in gradient wind. There is a substantial decrease in v_g throughout the troposphere in most of the eye and eyewall region, whereas there is an increase in v_g everywhere outwards of 70 km. The cooling in the midlevel eye is associated with the fact that the weakening of the gradient wind in the eye and eyewall is greatest in the lowest 2 km: that is, that the midlevel winds weaken *less* than those below. Finally, Fig. 16h shows the 24-h change in the actual tangential wind. Above 2 km, the changes in v qualitatively mirror those of v_g , as deviations from gradient balance are small. In the lowest 2 km, the magnitude of the change in v is much greater than that of v_g ; the difference represents tendencies in the unbalanced flow, and these tendencies therefore do not correspond to tendencies in $\partial T / \partial r$. The change in the unbalanced wind is the component of the tangential wind tendency that is most visually apparent when comparing Fig. 12f to Fig. 12h and yet bears no relationship to the change in the temperature field and therefore the structure of the warm core.

The above analysis and the analysis of SN12 indicate why it is so difficult to draw general conclusions regarding the structural relationships between the warm core and the wind field. Above the boundary layer, thermal wind balance is a good approximation, and the warm core is closely related to the wind structure. However, what we observe as the warm core in the eye is the integrated effect of radial temperature gradients throughout the TC, so temperature changes in the eye need not relate to wind changes in the eyewall or at any particular radius. Without knowing the full radius–height structure of both the temperature and wind fields, we cannot easily relate changes in one to changes in the other. With model data, we can begin to more carefully investigate structural relationships, as we did above. However, even in this case, the interpretation is challenging, and it remains difficult to make specific associations between the warm-core structure of the eye and the overall wind structure.

5. Discussion

SN12 and SZ13a,b found that, in their idealized simulations, the warm core was consistently maximized between 4- and 8-km height. They also found no

evidence that the height of the maximum varied systematically with storm intensity. In this investigation of Earl, the warm core (both observed and simulated) is sometimes found to be higher than in SN12. Nevertheless, when using a local environmental reference, a midlevel maximum in perturbation temperature often occurs, consistent with SN12. Importantly, there is no systematic relationship between the height of the warm core and intensity or intensity change in Earl, also consistent with SN12.

As noted in the introduction, Chen et al. (2011) and Chen and Zhang (2013) argued that the upper-level (14 km) warm-core maximum they found in their Wilma simulation was responsible for Wilma's extreme intensity, and, had the maximum not been so high, Wilma would not have been so strong. It is difficult to determine why their simulated Wilma had the maximum perturbation temperature at a much greater height than the idealized simulations of SN12. However, we believe that it is incorrect to attribute storm intensity to the height of the warm core in this manner. SN12 extensively discussed this idea, which we briefly summarize below.

It is true that, for a given temperature perturbation, the associated hydrostatic surface pressure anomaly is greater when the temperature perturbation is at a lower pressure (greater height). However, a given surface pressure anomaly can be associated with an essentially infinite combination of vertical temperature profiles, and there is no reason for presuming a particular profile. Wilma's extremely low surface pressure could potentially have been associated with an even warmer anomaly whose maximum was at a lower height, so it cannot be said that Wilma was stronger than it otherwise would have been because of the height of the maximum perturbation temperature. Indeed, that SN12 simulated extremely intense TCs with midlevel maxima implies that a maximum at 14-km height is not necessary to produce a category-5 hurricane. We note that Chen and Zhang (2013) performed a sensitivity test where they decreased the SST by 1°C everywhere and repeated their simulation. This resulted in a substantially weakened storm, with P_{\min} at peak intensity 37 mb higher than for their control simulation. However, the warm-core maximum for this weaker storm was again at about 14-km height, which seems contrary to the idea that the height of the warm core is important for determining storm intensity. It remains possible that there is some relationship between the height of the maximum perturbation temperature and storm intensity in real TCs, as was found in Durden (2013). However, hydrostatic balance does not require that there *must* be such a relationship.

Chen and Gopalakrishnan (2015, hereinafter CG15) simulated Hurricane Earl from 1800 UTC 26 August to

1800 UTC 31 August, encompassing the period prior to RI as well as the first period of RI. We investigate the period from 0600 UTC 29 August to 0000 UTC 3 September, so our timeframe only partially overlaps with that of CG15. During the period of maximum intensity, CG15 found that the maximum perturbation temperature was at 8-km height. Though CG15 compare this favorably to the Wilma simulation of Chen and Zhang (2013), the structure and evolution of the warm core in their simulated Earl is actually quite different from their simulated Wilma. The peak warm core in their Earl is 6 km lower than that in their Wilma. In CG15, the sudden onset of warming above 8-km height coincident with RI is contrasted with warming generally being confined to heights below 8 km prior to RI. Different from the Earl simulation of CG15, a sudden increase in depth of the layer with warming for Wilma is not evident in Fig. 1 of Chen and Zhang (2013); warming throughout the troposphere occurred prior to RI. Chen and Zhang (2013) emphasized the fact that the warm-core maximum elevated from 12 to 14 km during the RI of the simulated Wilma. Though somewhat noisy, the warm-core maximum in CG15 appears to elevate from 6 to 8 km during the RI of the simulated Earl. CG15 do not mention this, however, instead emphasizing the increase in depth of the layer of overall warming. As our simulation begins at the onset of RI, we cannot directly compare our simulation to theirs regarding their finding that the depth over which there is warming increases during RI. However, we can see that, during the 60-h period of overlap (0600 UTC 29 August–1800 UTC 31 August) of our respective simulations, the height of maximum perturbation temperature is roughly comparable, given differences in how we define the reference temperature profile. Additionally, the temperature increases during RI throughout the depth of the troposphere in both our simulation and that of CG15, and both simulations are qualitatively consistent with the dropsonde observations in this respect.

CG15 examine the hydrostatic contribution of warming above and below 8-km height to the surface pressure perturbation and find that warming above 8 km contributes 45 mb to the pressure fall in Earl. From this, they argue that “RI would not have occurred” without the warming above 8 km. This type of analysis presumes that tropical cyclone intensity is causally driven by the warming of the eye itself, which we think is likely incorrect. It is generally accepted that (above the boundary layer) the temperature field is in approximate balance with the tangential wind field, so changes in either field will lead to changes in the other. This adjustment to thermal wind balance is very rapid, and it is very difficult to determine whether the wind is adjusting

to the temperature, or vice versa. Indeed, in the widely accepted convective ring model of tropical cyclone spinup, warming of the eye and intensification of the wind field occur simultaneously. The idea that warming of the eye itself is the fundamental determinant of storm intensity is also inconsistent with the potential intensity theory of Emanuel (1986). Emanuel’s theory is based on the idea that TCs intensify as a result of a positive feedback between surface heat fluxes and surface winds. The theoretical maximum winds at the top of the boundary layer are determined irrespective of the distribution and magnitude of eye warming, and the eye warming is only determined after solving for the maximum winds. Of course, this inconsistency does not necessarily falsify the idea that eye warming itself is the fundamental agent of intensification. However, there is currently little evidence for this idea, so we think it is misleading to focus on the height of maximum warming as a key aspect of intensity and intensity change.

CG15 also compared their simulated RMW to the observed, and we would like to point out a discrepancy between our respective results. CG15 found that their simulation predicted an RMW that was similar to observed at most times, particularly in the period prior to RI. They noted that the simulated RMW contracted from about 50 to 20–30 km in the period from 0600 to 1200 UTC 29 August, “consistent with the observations.” While it is true that their simulation is similar to the extended best-track (EBT) data (that they rely on) in this respect, the EBT data are themselves inconsistent with the observed azimuthal mean wind fields that we presented. As we showed (Fig. 3a), the radar-analyzed RMW was 95 km at 2-km height at 1200 UTC 29 August [and this is also consistent with the analysis presented in Rogers et al. (2015)]. This RMW contracts greatly by 0000 UTC 30 August (Fig. 3b), a time period for which the EBT instead indicates expansion. It seems possible that the EBT RMW at 1200 UTC 29 August is reflective of an inner relict RMW that is evident in the azimuthal mean wind field (Fig. 3a) as well as the horizontal cross section at 2 km (Fig. 2a). It is apparent, however, that the RMW that is actually associated with the inner core of Earl during RI originates from a contraction of the larger RMW, rather than an expansion of the weaker relict RMW. Therefore, it is possible that the correspondence of the simulated RMW of CG15 with observations is, in part, related to uncertainties or errors in the EBT dataset.

As mentioned in the introduction, several recent studies (SN12; SZ13a; Wang and Wang 2014; Ohno and Satoh 2015) have found distinct mid- and upper-level maxima in perturbation temperature, with the upper-level maximum forming only once a TC is relatively

intense (category 2 or 3). From a potential temperature θ budget, SZ13a found that the upper-level maximum in perturbation temperature was a consequence of a similar local maximum in azimuthal mean vertical advective warming that occurred during the latter portion of RI. Mean descent near the center during intensification was consistently an absolute maximum at 12–13-km height, slightly below the height of the upper-level perturbation temperature maximum. Though this persistent descent was substantially stronger than that at midlevels, the midlevel warm core remained stronger in SZ13a, because the static stability was very weak at the level of peak descent, so relatively less warming could be accomplished by vertical advection.

In SZ13a, we attributed the overall vertical structure of the warm core in our simulations to the structure of static stability in the mean tropical troposphere: there is a local maximum in stability at midlevels, so relatively weak descent can accomplish substantial warming, whereas stability is very weak in the upper troposphere from 8 to 12 km, leading to a decrease of warming with height in this region. Static stability rapidly increases with height above about 13 km, in the tropical tropopause layer (TTL), and SZ13a concluded that the secondary maximum in perturbation temperature at 12–14-km height was a result of this stability structure. In Wang and Wang (2014) and Ohno and Satoh (2015), the upper-level maximum became stronger than the midlevel maximum, in contrast to SZ13a. We speculate that, in their simulations, there may have been greater descent in the high-stability tropical tropopause region than in SZ13a, leading to greater warming, and a relatively stronger upper-level maximum. Whether the mid- or upper-level maximum is stronger likely depends on subtle details of the vertical profiles of vertical velocity and static stability. In any case, the existence of dual maxima in Wang and Wang (2014) and Ohno and Satoh (2015) is consistent with the argument of SZ13a that the structure of the warm core is strongly related to the structure of the mean environmental static stability.

Further evidence for the influence of environmental static stability on warm-core structure can be seen in Fig. 17, which compares the static stability N^2 in the environments of the observed and simulated Earl, as well as in the Dunion mean sounding. To reduce the noise in observed profiles, we calculate $N^2 = (g/\theta)(\partial\theta/\partial z)$ for each G-IV sonde that is 300–700 km from the center, average all such sondes for each day, and then average these four profiles. For the simulation, we average the same quantity between 300–700 km and over the same four times shown in Figs. 13 and 14. In general, there is a very good correspondence between

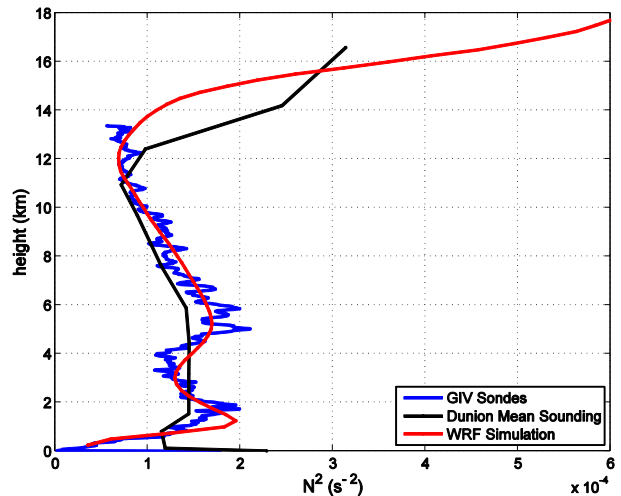


FIG. 17. Static stability N^2 vs height for the G-IV dropsondes, the Dunion mean sounding, and the WRF simulation. For the dropsondes and the simulation, the profiles that are shown are the means between 300- and 700-km radius averaged over four days. Details are given in the text.

the observed and simulated N^2 in the near-storm environment. In both, there are maxima at 1.5–2 and 5–6 km, a local minimum at 3–4 km, and an essentially monotonic decrease from 6- to 12-km height. It is likely that this midlevel maximum in environmental N^2 is at least, in part, responsible for the tendency for a maximum in perturbation temperature to form at similar heights in the eye of Earl. The temporal variability in the environment (not shown) is relatively small, so the differences in the prominence or existence of the midlevel warm-core maximum on different days within the observations, as well as differences between the simulation and observations, are likely a function of the dynamics of the eye. Although SZ13a,b showed that a number of processes make important contributions to the evolution of temperature within the eye of TCs, at most times it is the azimuthal mean vertical advection of potential temperature that is dominant. Therefore, it is most likely that the variation in the height of the absolute maximum of perturbation temperature in Earl is associated with variations in the vertical profile of azimuthal mean vertical velocity within the eye. The budget analyses required to determine this are beyond the scope of this study (and not possible for the observations). Nevertheless, we can speculate that the disappearance of the previously observed midlevel maximum on 1 September is associated with some combination of increased subsidence above 6 km and decreased subsidence below within the eye during the ERC. The temporal and interstorm variability in the vertical profile of mean vertical velocity in the eye,

which is itself dependent on static stability, is currently poorly understood.

In Earl, there is clear evidence of dual maxima in perturbation temperature from the dropsonde observations, especially when using a local environmental reference state. While the midlevel maximum is found at comparable heights as seen in the simulations of SN12 and SZ13a, the upper-level maximum is observed at 9–12 km, which is lower than that found in the aforementioned studies (12–14 km) and substantially lower than the 15–16-km maxima found by Wang and Wang (2014) and Ohno and Satoh (2015). At least some of the time in Earl (particularly on 2 September), however, the perturbation temperature is increasing with height at the top of the dropsonde profile (11–12 km), so the true maximum is likely above flight level and unsampled. Durden (2013) found the height of peak perturbation temperature to be quite variable among the storms in his dataset, so it is perhaps unsurprising that there is a lack of consistency in this respect between the Earl observations and various idealized and real-data numerical studies. Nonetheless, the existence of the dual maxima in the observations affirms that such a simulated characteristic of TCs is at least broadly realistic. This is not the first such observation of dual warm-core maxima; as noted in the introduction, Hawkins and Imbembo (1976) found two distinct maxima in Hurricane Inez (1966), though they believed that such a phenomenon was “rather unusual.” Though there are still not enough observations of warm-core structure to ascertain the frequency of such an occurrence, it now seems likely that simultaneous mid- and upper-level maxima of perturbation temperature in intense tropical cyclones are relatively common.

In this study, we have shown that both the height of the absolute maximum perturbation temperature and the overall shape of the profile can be quite sensitive to the chosen reference profile, consistent with the results of SN12 and Durden (2013). Therefore, it is critical that future studies of the warm core make clear their choice of reference profile. Ideally, the reference profile should be similar to that of any previous studies with which comparisons are being made. Aside from purposes of comparison, the reference that is most appropriate depends on the research focus. Although any choice remains somewhat arbitrary, the wind field is dynamically related to the local environment and not to a mean tropical sounding. Therefore, for trying to understand the relationship between the warm core and the TC circulation, we believe that a local environmental reference state is most appropriate. On the other hand, for simply evaluating changes in temperature with time within a given storm, a fixed profile, such as the

Dunion sounding, is more useful, as changes in perturbation temperature will correspond to changes in actual temperature.

6. Summary

We presented an observational analysis of the warm-core structure of Hurricane Earl (2010) on four different days using high-altitude dropsondes from the DC-8 aircraft. To supplement this analysis, we also examined the evolution of the wind field using Doppler wind analyses from the NOAA P-3 aircraft. We calculated the perturbation temperature using two different definitions of the environment: 1) the Dunion (2011) moist tropical mean sounding and 2) the actual near environment of Earl, as obtained from NOAA G-IV dropsondes. Between the first two DC-8 flights (during RI), the temperature of the eye warmed at all heights below 12 km. Warming continued between the second and third flights, though mostly above 6-km height. Between the third and fourth flights, the eye temperature did not change substantially, in spite of a 30-kt decrease of the maximum winds and 17-mb increase in minimum pressure during this period. Through hydrostatic balance, this implies that there must have been (unsampled) cooling in a layer above 12-km height that was associated with this pressure rise.

The height of the maximum perturbation temperature in Earl is at times very sensitive to the choice of reference profile, which is a consequence of the fact that the difference between the Dunion and G-IV temperature increases with height. For three of the flights (29 and 30 August and 2 September), using the G-IV soundings as the environmental profile gives two distinct maxima in perturbation temperature of roughly equal magnitude: one at midlevels (4–6 km) and the other at upper levels (9–12 km). In contrast, the midlevel maxima are all weaker than the upper-level maxima when instead using the Dunion profile as the environment. We found no obvious systematic relationship between the height of the warm core in Earl and either intensity or intensity change.

To complement our observational analyses, we examined the warm-core structure and evolution for a WRF forecast of Earl and additionally compared the forecast wind structure to the Doppler analyses. Overall, the magnitude and the vertical structure of the forecast warm core compare well with the observations, especially for the first two days (29 and 30 August). On 29 August, the broad maximum in perturbation temperature from 7- to 10-km height is well forecast, as is the rapid increase of perturbation temperature with height from 3 to 7 km. Similarly, on 30 September, the

overall pattern of warm-core magnitude and vertical structure is well forecast. There are relatively small (1° – 2°C) but noticeable temperature biases, and these are likely attributable to slight intensity biases. Between 30 August and 1 September, an ERC occurred that was not forecast, and, as a result, there are more substantial structural differences between the model and observations than were present at shorter lead times. In particular, the forecast RMW at mid and upper levels was much too large on 1 September, and this likely contributed to the existence of a midlevel absolute maximum in perturbation temperature that was not observed. On 2 September, the forecast vertical profile of perturbation temperature is more similar to the observed, although at this time there is an observed midlevel maximum, whereas the forecast has a broad maximum over a deeper layer. It is clear that a good intensity forecast does not guarantee a good forecast of either warm-core structure or wind structure. Nevertheless, it is also evident that good forecasts of warm-core structure are possible at lead times of 1–2 days and that, even at 4 or 5 days, decent predictions of warm-core structure are possible, even when significant intermediary structural changes, such as ERCs, are entirely missed.

Acknowledgments. This research was partially supported by NASA (Grant NNX12AJ79G), ONR (Grants N000140910526, 0601153N, and 0602435N), NOAA (HFIP), and NSF (Grant 063064). This research was performed in part at NCAR while the first author was an NSF-AGS Postdoctoral Fellow (Award 1231193). Simulations were performed at the Texas Advanced Computing Center (TACC). We thank Yonghui Weng for running the WRF simulations. We thank Jon Poterjoy for providing helpful comments and suggestions on an earlier version of this manuscript. We thank NASA and NCAR/EOL for making available the GRIP dropsonde dataset, NOAA/HRD for making available the Doppler radar analyses and G-IV dropsondes, and University of Wisconsin/CIMSS for allowing us to use their satellite montage image. We are grateful for the comments and suggestions of three anonymous reviewers, which resulted in substantial improvements in this manuscript.

REFERENCES

- Braun, S. A., and Coauthors, 2013: NASA's Genesis and Rapid Intensification Processes (GRIP) field experiment. *Bull. Amer. Meteor. Soc.*, **94**, 345–363, doi:10.1175/BAMS-D-11-00232.1.
- Cangialosi, J. P., 2011: Tropical cyclone report: Hurricane Earl. National Hurricane Center Tropical Cyclone Rep. AL072010, 29 pp. [Available online at http://www.nhc.noaa.gov/data/tcr/AL072010_Earl.pdf.]
- Chen, H., and D.-L. Zhang, 2013: On the rapid intensification of Hurricane Wilma (2005). Part II: Convective bursts and the upper-level warm core. *J. Atmos. Sci.*, **70**, 146–162, doi:10.1175/JAS-D-12-062.1.
- , and S. G. Gopalakrishnan, 2015: A study on the asymmetric rapid intensification of Hurricane Earl (2010) using the HWRF system. *J. Atmos. Sci.*, **72**, 531–550, doi:10.1175/JAS-D-14-0097.1.
- , D.-L. Zhang, J. Carton, and R. Atlas, 2011: On the rapid intensification of Hurricane Wilma (2005). Part I: Model prediction and structural changes. *Wea. Forecasting*, **26**, 885–901, doi:10.1175/WAF-D-11-00001.1.
- Dunion, J. P., 2011: Rewriting the climatology of the tropical North Atlantic and Caribbean Sea atmosphere. *J. Climate*, **24**, 893–908, doi:10.1175/2010JCLI3496.1.
- Durden, S. L., 2013: Observed tropical cyclone eye thermal anomaly profiles extending above 300 hPa. *Mon. Wea. Rev.*, **141**, 4256–4268, doi:10.1175/MWR-D-13-00021.1.
- Emanuel, K. A., 1986: An air–sea interaction theory for tropical cyclones. Part I: Steady-state maintenance. *J. Atmos. Sci.*, **43**, 585–604, doi:10.1175/1520-0469(1986)043<0585:AASITF>2.0.CO;2.
- Gamache, J. F., J. S. Griffin Jr., P. P. Dodge, and N. F. Griffin, 2004: Automatic Doppler analysis of three-dimensional wind fields in hurricane eyewalls. *26th Conf. on Hurricanes and Tropical Meteorology*, Miami, FL, Amer. Meteor. Soc., 5D.4. [Available online at <http://ams.confex.com/ams/pdfpapers/75806.pdf>.]
- Green, B. W., and F. Zhang, 2013: Impacts of air–sea flux parameterizations on the intensity and structure of tropical cyclones. *Mon. Wea. Rev.*, **141**, 2308–2324, doi:10.1175/MWR-D-12-00274.1.
- Halverson, J. B., J. Simpson, G. Heymsfield, H. Pierce, T. Hock, and L. Ritchie, 2006: Warm core structure of Hurricane Erin diagnosed from high altitude dropsondes during CAMEX-4. *J. Atmos. Sci.*, **63**, 309–324, doi:10.1175/JAS3596.1.
- Hawkins, H. F., and D. A. Rubsam, 1968: Hurricane Hilda, 1964. Part II: Structure and budgets of the hurricane core on 1 October 1964. *Mon. Wea. Rev.*, **96**, 617–636, doi:10.1175/1520-0493(1968)096<0617:HH>2.0.CO;2.
- , and S. M. Imbombo, 1976: The structure of a small, intense Hurricane—Inez 1966. *Mon. Wea. Rev.*, **104**, 418–442, doi:10.1175/1520-0493(1976)104<0418:TOSASI>2.0.CO;2.
- Jordan, C. L., 1958: Mean soundings for the West Indies area. *J. Meteor.*, **15**, 91–97, doi:10.1175/1520-0469(1958)015<0091:MSFTWI>2.0.CO;2.
- Jorgensen, D. P., P. H. Hildebrand, and C. L. Frush, 1983: Feasibility test of an airborne pulse-Doppler meteorological radar. *J. Appl. Meteor. Climatol.*, **22**, 744–757, doi:10.1175/1520-0450(1983)022<0744:FTOAAAP>2.0.CO;2.
- Knaff, J. A., S. A. Seseke, M. DeMaria, and J. L. Demuth, 2004: On the influences of vertical wind shear on symmetric tropical cyclone structure derived from AMSU. *Mon. Wea. Rev.*, **132**, 2503–2510, doi:10.1175/1520-0493(2004)132<2503:OTIOVW>2.0.CO;2.
- La Seur, N. E., and H. F. Hawkins, 1963: An analysis of Hurricane Cleo (1958) based on data from research reconnaissance aircraft. *Mon. Wea. Rev.*, **91**, 694–709, doi:10.1175/1520-0493(1963)091<0694:AAOHCB>2.3.CO;2.
- Nolan, D. S., D. P. Stern, and J. A. Zhang, 2009: Evaluation of planetary boundary layer parameterizations in tropical cyclones by comparison of in situ observations and high-resolution simulations of Hurricane Isabel (2003). Part II: Inner-core boundary layer and eyewall structure. *Mon. Wea. Rev.*, **137**, 3675–3698, doi:10.1175/2009MWR2786.1.

- , R. Atlas, K. T. Bhatia, and L. R. Bucci, 2013: Development and validation of a hurricane nature run using the joint OSSE nature run and the WRF Model. *J. Adv. Model. Earth Syst.*, **5**, 382–405, doi:10.1002/jame.20031.
- Ohno, T., and M. Satoh, 2015: On the warm core of a tropical cyclone formed near the tropopause. *J. Atmos. Sci.*, **72**, 551–571, doi:10.1175/JAS-D-14-0078.1.
- Reasor, P. D., M. D. Eastin, and J. F. Gamach, 2009: Rapidly intensifying Hurricane Guillermo (1997). Part I: Low-wavenumber structure and evolution. *Mon. Wea. Rev.*, **137**, 603–631, doi:10.1175/2008MWR2487.1.
- Rogers, R. F., P. D. Reasor, and J. A. Zhang, 2015: Multiscale structure and evolution of Hurricane Earl (2010) during rapid intensification. *Mon. Wea. Rev.*, **143**, 536–562, doi:10.1175/MWR-D-14-00175.1.
- Schubert, W. H., C. M. Rozoff, J. L. Vigh, B. D. McNoldy, and J. P. Kossin, 2007: On the distribution of subsidence in the hurricane eye. *Quart. J. Roy. Meteor. Soc.*, **133**, 595–605, doi:10.1002/qj.49.
- Stern, D. P., 2010: The vertical structure of tangential winds in tropical cyclones: Observations, theory, and numerical simulations. Ph. D. dissertation, University of Miami, 455 pp. [Available online at http://scholarlyrepository.miami.edu/cgi/viewcontent.cgi?article=1444&context=oa_dissertations.]
- , and D. S. Nolan, 2009: Reexamining the vertical structure of tangential winds in tropical cyclones: Observations and theory. *J. Atmos. Sci.*, **66**, 3579–3600, doi:10.1175/2009JAS2916.1.
- , and —, 2012: On the height of the warm core in tropical cyclones. *J. Atmos. Sci.*, **69**, 1657–1680, doi:10.1175/JAS-D-11-010.1.
- , and F. Zhang, 2013a: How does the eye warm? Part I: A potential temperature budget analysis of an idealized tropical cyclone. *J. Atmos. Sci.*, **70**, 73–90, doi:10.1175/JAS-D-11-0329.1.
- , and —, 2013b: How does the eye warm? Part II: Sensitivity to vertical wind shear and a trajectory analysis. *J. Atmos. Sci.*, **70**, 1849–1873, doi:10.1175/JAS-D-12-0258.1.
- , J. R. Brisbois, and D. S. Nolan, 2014: An expanded dataset of hurricane eyewall sizes and slopes. *J. Atmos. Sci.*, **71**, 2747–2762, doi:10.1175/JAS-D-13-0302.1.
- Wang, H., and Y. Wang, 2014: A numerical study of Typhoon Megi (2010). Part I: Rapid intensification. *Mon. Wea. Rev.*, **142**, 29–48, doi:10.1175/MWR-D-13-00070.1.
- Weng, Y., and F. Zhang, 2012: Assimilating airborne Doppler radar observations with an ensemble Kalman filter for convection-permitting hurricane initialization and prediction: Katrina (2005). *Mon. Wea. Rev.*, **140**, 841–859, doi:10.1175/2011MWR3602.1.
- Willoughby, H. E., and M. B. Chelmon, 1982: Objective determination of hurricane tracks from aircraft observations. *Mon. Wea. Rev.*, **110**, 1298–1305, doi:10.1175/1520-0493(1982)110<1298:ODOHTF>2.0.CO;2.
- Wu, L., S. A. Braun, J. Halverson, and G. Heymsfield, 2006: A numerical study of Hurricane Erin (2001). Part I: Model verification and storm evolution. *J. Atmos. Sci.*, **63**, 65–86, doi:10.1175/JAS3597.1.
- Young, K., J. Wang, T. Hock, and D. Lauritsen, 2011: Genesis and Rapid Intensification Processes (GRIP) 2010 quality controlled dropsonde dataset. NASA Earth Observing System Data and Information System, accessed September 2013. [Available online at 10.5067/GRIP/DROPSONDE/DATA201.]
- Zhang, F., and Y. Weng, 2015: Predicting hurricane intensity and associated hazards: A five-year real-time forecast experiment with assimilation of airborne Doppler radar observations. *Bull. Amer. Meteor. Soc.*, **96**, 25–33, doi:10.1175/BAMS-D-13-00231.1.
- Zhang, J. A., and F. D. Marks, 2015: Effects of horizontal diffusion on tropical cyclone intensity change and structure in idealized three-dimensional numerical simulation. *Mon. Wea. Rev.*, **143**, 3981–3995, doi:10.1175/MWR-D-14-00341.1.
- , D. S. Nolan, and R. F. Rogers, 2015: Evaluating the impact of improvements in the boundary layer parameterization on hurricane intensity and structure forecasts in HWRF. *Mon. Wea. Rev.*, **143**, 3136–3155, doi:10.1175/MWR-D-14-00339.1.